ADVANCED FUNCTIONAL MATERIALS
www.afm-journal.de

Bioinspired Shape Reconfigurable, Printable, and Conductive "E-Skin" Patch with Robust Antibacterial Properties for Human Health Sensing

*Hojin Kim, Sayan Deb Dutta, Myoung Joon Jeon, Jieun Lee, Hyeonseo Park, Youjin Seol, and Ki-Taek Lim**

Conductive hydrogel-based flexible electronic skin, or "E-skin," patches have garnered significant attention in biomedical engineering due to their capability to sense and detect real-time human motion, health metrics, and environmental changes. Nonetheless, challenges such as precision fabrication, enhanced flexibility, superior self-healing, hydrophilicity, and insufficient bioadhesive properties impede their clinical application and limit their advancement in wearable bioelectronics. In this context, the development of a highly flexible, shape-reconfigurable, stretchable, and printable conductive "E-skin" patch for real-time human motion, humidity, and temperature sensing. This utilizes a polyvinyl alcohol/gelatin/carbon nanotubes/cellulose nanocrystals (PVA/Gelatin/CNTs/CNCs or PVG/NC) based hydrogel inspired by slime molds. Modifying PVG with CNTs and CNCs enhances the mechanical and viscoelastic properties, thereby facilitating high-resolution direct ink writing (DIW) based 3D printing. The resulting slime-like "E-skin" demonstrates an electrical conductivity of ≈5 ± 0.25 S m^{-1}, with exceptional stretchability (≈1000%). The nanocomposite "E-skin" also displays outstanding bioadhesive properties and multiple sensing capabilities for human motion, temperature, and humidity under ambient conditions. Furthermore, the PVG/NC showcases remarkable near-infrared (NIR) responsive attributes, which can be leveraged for eradicating pathogenic bacteria in chronic wounds and exhibit excellent cytocompatibility. This research holds immense promise for future wearable bioelectronics, particularly for non-invasive medical diagnostics.

1. Introduction

Conductive hydrogel-based bioelectronics is actively being researched in various fields, including motion detection, sports analysis, biometric data analysis, and biomedical engineering.[1] They offer broader applicability, lower costs, greater environmental friendliness, and superior performance compared to mechanical devices. Among them, hydrogels that adhere to the body like skin to collect data are known as "electronic skin" or "E-skin" patches. The "E-skin" patch is an electronic patch that mimics human skin and is actively researched in modern healthcare and medical fields, including health monitoring devices, smart drug delivery, and nano-biosystems.[2] Conventional mechanical patches have several drawbacks, such as hindering movement, being rigid and heavy, requiring replacement when damaged (=often generating crack), lacking antibacterial properties, and relying on traditional manufacturing and assembly methods. To address these limitations, "E-skin" patches of soft hydrogels derived from conductive nanomaterials and polymers would provide high flexibility, stretchability, and strong adhesion with outstanding self-healing properties.[3] Enhancing the conductivity of soft hydrogel-based "E-skin" is also one of the key factors for practical applications.[4] To achieve efficient and rapid signal transmission with high performance, materials such as silver nanowires (AgNWs),[5] liquid metals,[6] carbon nanotubes (CNT),[3,7] polyaniline,[8] poly3,4-ethylenedioxythiophene

---

H. Kim, S. D. Dutta, M. J. Jeon, J. Lee, H. Park, Y. Seol, K.-T. Lim
Department of Biosystems Engineering
Kangwon University
Chuncheon, Gangwon-do 24341, Republic of Korea
E-mail: ktlim@kangwon.ac.kr

The ORCID identification number(s) for the author(s) of this article can be found under https://doi.org/10.1002/adfm.202504088

DOI: 10.1002/adfm.202504088

H. Kim, M. J. Jeon, J. Lee, H. Park, Y. Seol, K.-T. Lim
Interdisciplinary Program in Smart Agriculture
Kangwon National University
Chuncheon, Gangwon-do 24341, Republic of Korea

S. D. Dutta, K.-T. Lim
Institute of Forest Science
Kangwon National University
Chuncheon, Gangwon-do 24341, Republic of Korea

S. D. Dutta
School of Medicine
University of California Davis
Sacramento 95817, USA

(PEDOT: PSS),[3,9] transition metal carbide or nitride (MXene),[10] and graphene oxide (GO)[11] are frequently used. The conductive nanomaterials or biopolymers can be mixed with naturally derived biocompatible materials to improve their stretchability, sensitivity, and biocompatibility towards "E-skin" development.[12]

Recently, cellulose and nanocellulose-based biomaterials have gained significant attention in developing flexible sensors due to their remarkable mechanical strength, high surface area-to-volume ratio, excellent electrical conductivity, and superior biocompatibility.[13] Cellulose nanocrystals (CNCs), a type of nanocellulose, improve durability, water retention, and electrical conductivity when incorporated into hydrogels.[14] For instance, Li et al. reported a CNC-based photonic hydrogel patch system for selective detection of calcium ions from human sweat.[15] This illustrates the advantages of CNC for body-attached patches, as it provides high toughness ($\approx$0.73 MJ m^{-3}), good adhesion, biocompatibility, and a reversible transition between dry and wet states. Furthermore, Hao et al. developed a hydrogel sensor with ultra-high tensile properties and a short response time (265 ms) using CNCs and CNT.[16] The dual reinforcement of CNCs and CNT enhances mechanical strength and electrical conductivity and displays near-infrared (NIR) responsive properties, which can be attributed to the improved antibacterial qualities of an "E-skin" patch.[17] Similarly, Shen et al. developed a strain sensor with good stretchability with ultra-low hysteresis (<1.5%) applicable to "E-skin" patches by combining PEDOT: PSS with polyvinyl alcohol (PVA).[9b] Due to their self-healing capabilities, Several efforts have been dedicated to creating PVA-based nanocomposite hydrogel sensors with adjustable properties.[18] CNTs can act as conductive nanofillers to enhance PVA's conductivity and mechanical properties.[19] However, CNTs exhibit potential toxicity to the human body at high concentrations (>2–3%), which limits their application in practice scenarios.[20] Additionally, CNCs are plant-derived biocompatible nanomaterials known for their excellent cytocompatibility and electrical conductivity[13,21] and can be used with CNTs to harness the potential toxicity of pure CNTs. Furthermore, most conductive hydrogels reported so far lack extreme self-healing capabilities and deform easily when stretched beyond 500%. Most fabricated "E-skin" patches depend on basic structural features, lacking the biomimicking properties of native skin.

Leveraging three-dimensional (3D) printing technology, it can fabricate complex biological structures using conductive materials hydrogels.[22] The 3D printing technique, widely used across various industries, has recently garnered attention in fabricating biomedical devices (e.g., soft probes and actuators), particularly in bioinspired designs for bioelectronics.[23] 3D printing enhances durability through uniform material distribution, making it a highly effective approach for "E-skin" patch development. For instance, Wu et al. demonstrated the fabrication of a conductive hydrogel using 3D printing for wearable strain sensing, customizing it to fit the shape of the hand joints.[24] Another study demonstrated superior sensing capabilities by 3D printing hydrogel in shapes customized for fingers and various body parts like the jaw, elbow, neck, wrist, and knee.[6] Nevertheless, increasing evidence highlighted the role of 3D printable conductive hydrogel patches for motion and temperature sensing applications.[19,25] This shows that 3D printed E-skin patches are suitable for motion sensing and detecting temperature, humidity, and sweat, highlighting their broad applicability and potential for diverse future applications.[6,26] Most current research concentrates on reactions to chemical cues such as perspiration and gases, along with mechanical stimuli like contact, compression, and bending. However, most components are restricted to paper or plastic substrates and require external power sources, which poses serious concerns and difficulties.[27] The potential of existing skin electrical components as valuable tools for health management is limited by this constraint. Prioritizing excellent machinability and efficient integration among stimulation–sensitive polymer networks is essential for advancing the development of adaptable hydrogel-based components designed for direct application on the body, ensuring superior biocompatibility and antimicrobial properties.

In this study, we designed a multifunctional, highly adhesive, stretchable, printable, and biocompatible hydrogel made of PVA/gelatin/MWCNT/CNCs (=PVG/NC) for sensing human body motion, temperature, and humidity aimed at innovative healthcare (**Scheme 1**). Recognizing the need for a biocompatible and bioadhesive "E-skin" with adjustable multifunctionality, we carefully selected PVA and gelatin as polymer matrices due to their high water solubility, unique molecular structure, self-healing properties, and dynamic crosslinking capability (including covalent, non-covalent, and inter- and intra-molecular hydrogen bonds), along with cost-effectiveness and a one-pot fabrication strategy. Gelatin, a hydrolysis product of collagen, is frequently used in tissue engineering owing to its skin extracellular matrix (ECM) mimicking properties with RGD (arginyl–glycyl–aspartic acid) adhesive domains, which shows a temperature-responsive gelation behavior.[28] Inspired by the slime mold,[29] which can variously re-shape its body, the developed PVG/NC hydrogel "E-skin" exhibits superior stretching ($\approx$1000%), recovery potential, elasticity, conductive ($\approx 5.38 \pm 0.25$ S m^{-1}), and antibacterial ($\approx$99%) against pathogenic bacteria. The dual reinforcement of PVG with MWCNT/CNC and dynamic crosslinking improved the viscoelasticity, adhesive, mechanical strength, and overall conductivity of the PVG/NC patch. Notably, the presence of PVA and gelatin offered high-resolution direct ink writing (DIW) based 3D printing under ambient conditions with varying geometries. Owing to the NIR-responsive property of the MWCNT, the PVG/NC "E-skin" showed good photothermal properties (up to 75 °C), which could be beneficial for treating infected skin wounds during chronic injury. Finally, we tested the sensing potential of the PVG/NC patch toward human body movement (wrist, finger, forehead, voice, hand gesture, and elbow joint), temperature (10–60 °C), and humidity (10–80%). The fabricated PVG/NC slime-like "E-skin" is non-invasive, mechanically robust, flexible, and biocompatible towards human skin cells (HaCaT), making it suitable as an "E-skin" patch. This study demonstrates a new perspective for developing soft and flexible "E-skin" patches for daily medical health management towards future bioelectronics.

2. Results and Discussion

2.1. Characterization of PVG/NC "E-Skin" Patches

Conductive hydrogels with dynamic crosslinking exhibit fluidity and flexibility, making them a primary material in various

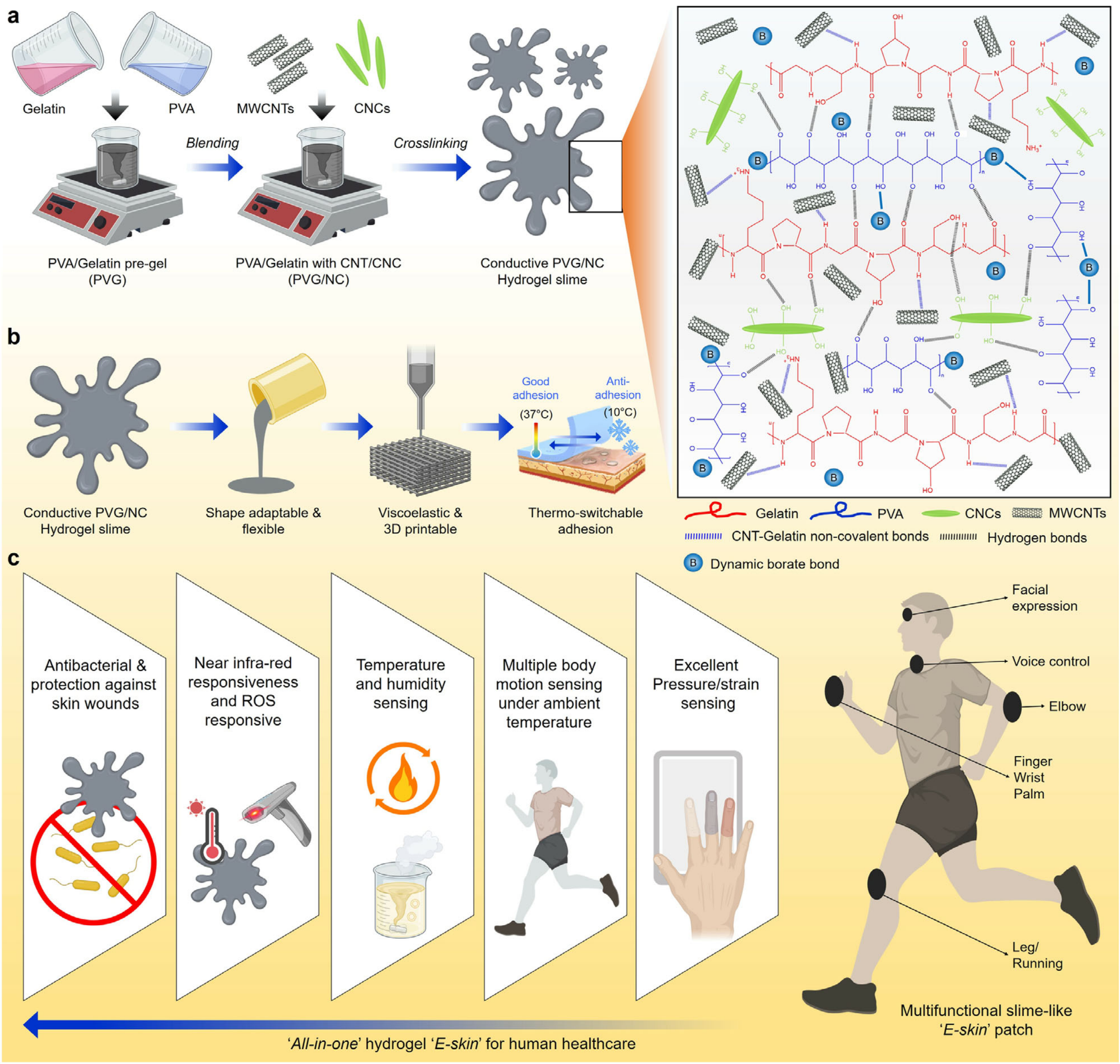

Scheme 1. Slime mold-inspired multifunctional "E-skin" hydrogel patch for human motion sensing and biological applications. a) Schematic illustration of the MWCNTs and CNCs dual-crosslinked semi-IPN hydrogel fabrication with dynamic bonds. b) The as-fabricated hydrogel has shape-adaptable properties with good printing and temperature-responsive adhesion/anti-adhesion properties. c) The "E-skin" patch exhibited NIR-responsive properties, which could be beneficial for antibacterial therapy with high electrical conductivity and especially helpful for multimodal sensing applications.

sensing applications. In nature, slime molds exhibit a similar ability to stretch and move freely in various forms in various substrates. Slime molds, multinucleated unicellular organisms, can move autonomously without physical limbs or muscles.[29] **Figure** 1a,b illustrates the slime mold's gripping and gliding image, which motivated us to fabricate a bio-inspired slime-like "E-skin" patch. The PVG/NC hydrogel was crosslinked with borax to introduce dynamic borate crosslinking within the polymer chains. Figure 1c displays the digital photograph of the fabricated PVG/NC hydrogel for multimodal applications. Owing to the presence of dynamic borate crosslinking and inter-/intra-molecular hydrogel bonding, the PVG/NC hydrogel exhibited superior shape adaptability (Figure 1c(i)) onto the human skin, which mimics the slime-mold body morphology and physiology. Besides the presence of gelatin chains, the "E-skin" patch displayed temperate-dependent adhesive properties, where the low temperature (≈4 ± 10 °C) facilitated anti-adhesion, while the body temperature (≈37 ± 2 °C) modulated the desirable skin adhesion (Figure 1c(ii)). Furthermore, the good adhesive behavior also showed a deformation-resistance property when stuck to the skin surface (Figure 1c(iii)) and underbody stretching, which is ideal for body-patchable biosensing application (Figure 1c(iv)). The excellent electrical conductivity of PVG hydrogel functionalized with MWCNTs/CNCs enables

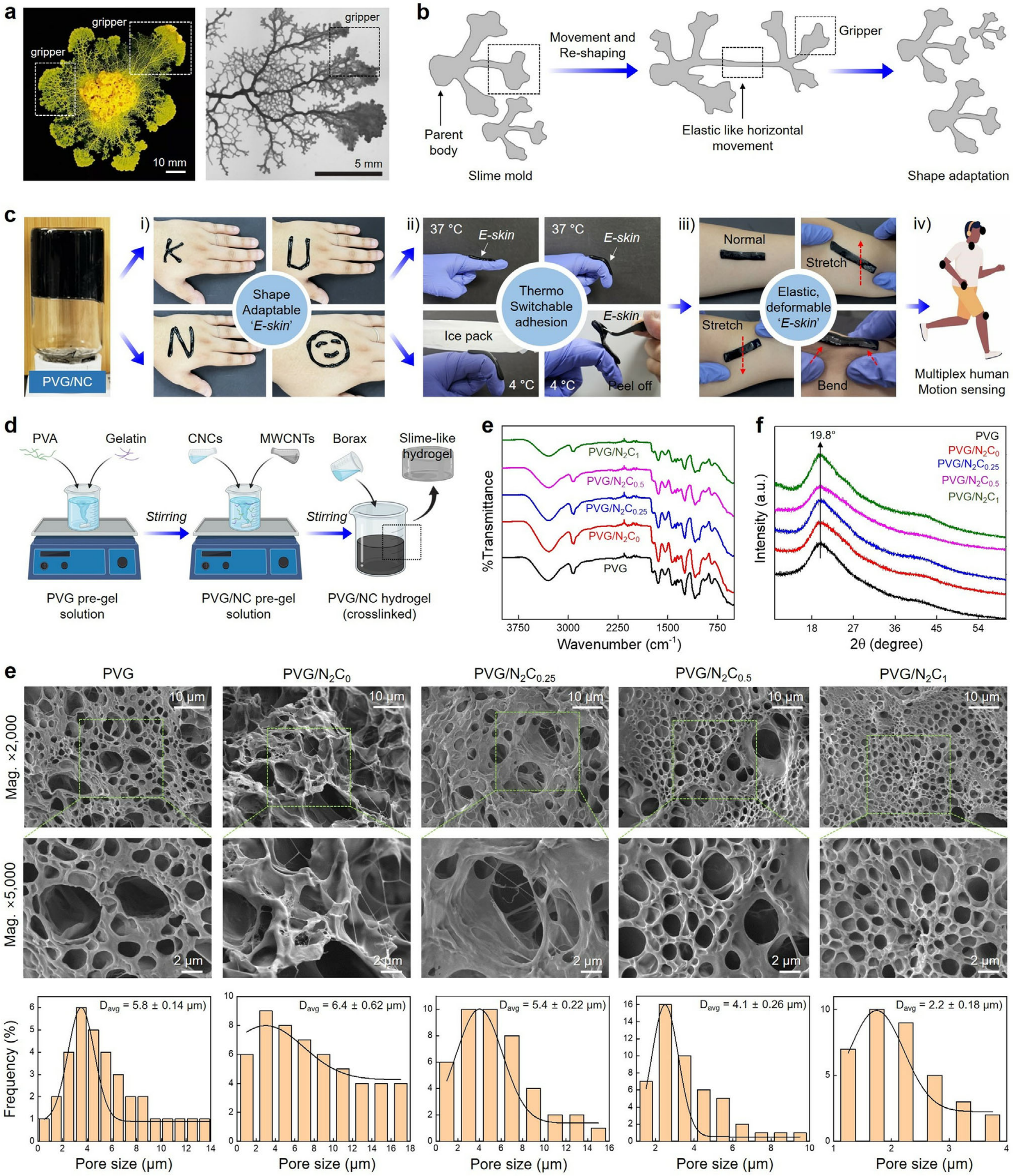

Figure 1. Fabrication and characterization of the slime mold-inspired "E-skin" patch for multimodal applications. a,b) The shape and movement of a slime mold growing in culture media. Scale bars: 5 and 10 mm.[29] c) PVG/NC hydrogel and its various functionalities: i) "E-skin" that can be fabricated in diverse forms; ii) "E-skin" that is easily attachable and detachable depending on temperature; iii) E-skin that maintains adhesion in dynamic conditions; and iv) "E-skin" capable of detecting various body motions. d) Schematic illustration of the fabrication method of PVG/NC hydrogel. e) FT–IR spectra of PVG and PVG/NC composites. f) XRD spectra of PVG and PVG/NC composites. g) FE–SEM images of freeze-dried PVG and PVG/NC nanocomposite scaffolds and their corresponding pore size distribution. scale bars: 2 and 10 μm.

higher conductivity and sensing ability during pressure-induced conditions. A schematic illustration of the PVG/NC hydrogel "E-skin" fabrication is shown in Figure 1d. We used rice husk-derived CNCs and MWCNTs for the nanocomposite hydrogel fabrication. The high-resolution transmission electron microscopy (TEM) images of the CNCs and MWCNTs are shown in Figure S1 (Supporting Information). The CNCs exhibited unique needle-like morphology with an average length and width of 109.72 ± 3.6 nm and 6.78 ± 0.21 nm (Figure S1a–c, Supporting Information), quite similar to our previous study.[30] Besides, the MWCNTs appear as filament-like structures with thick outer walls, indicating the distinct layers and the average thickness (= width) is calculated to be 9.25 ± 0.43 nm (Figure S1d,e, Supporting Information), respectively.

The chemical interaction and structural changes of the PVG hydrogel after the addition of CNT/CNC are evaluated using fourier-transform infrared (FT–IR) and X-ray diffraction (XRD) spectroscopy. Figure 1e shows a broad peak between 3200–3600 cm^{-1} corresponds to hydrogen bonded alcohols and phenols, indicating strong O—H stretching vibrations. This demonstrates that PVA forms strong hydrogen bonds with gelatin residues.[31] Peaks in the range of 2850–2970 cm^{-1} represent alkanes, showing strong C—H bonds, which indicate that the carbon in CNT is well bonded with PVA. The peak ≈1643 cm^{-1} corresponds to C═C bonds, while the peaks in the 1000–1250 cm^{-1} range represent C—O—C, C—HO, and C—H bonds. This confirms that the hydrogel exhibits strong molecular bonding with gelatin and/or CNCs or CNTs.[32] Figure 1f depicts the XRD pattern of freeze-dried PVG/NC hydrogel films. The hydrogels exhibited a characteristic diffraction peak at $2\theta = 19.8°$, corresponding to the amorphous structure of PVA. As the CNC and/or MWCNT content increased, the intensity of the diffraction peak also increased, and the peak became sharper, indicating improved crystal formation. The higher CNC content enhanced the stability of the polymer chains, as CNC acted as a crosslinking node, enabling the hydrogel to achieve greater mechanical strength.

The morphology of the freeze-dried PVG/NC hydrogel scaffolds was evaluated through field-emission scanning electron microscope (EF-SEM), and the results are shown in Figure 1g. The pure PVG scaffold exhibited unique micro and macroporous morphology distributed throughout the surface. Notably, after CNT incorporation, the PVG/N$_2$C$_0$ scaffold displayed flaky porous morphology with periodic fibrillar structures. The higher magnification images of the scaffolds are shown in Figure S2a–e (Supporting Information). More interestingly, as the CNC content increased from 0.25 → 1 wt.% in the PVG/CNT matrix, the flaky morphology disappeared, and more ordered porosity was noticed. The increasing content of CNC in the PVG/CNT matrix allowed more significant interaction and, thereby, uniform ice crystal formation during freezing, resulting in uniform porosity.[33] The PVG/N$_2$C$_{0.5}$ and PVG/N$_2$C$_1$ displayed the most uniform porosity among the various formulations. The low-resolution SEM image of the PVG/N2C1 scaffold surface morphology is shown in Figure S2f (Supporting Information). The average pore size of the PVG, PVG/N$_2$C$_0$, PVG/N$_2$C$_{0.25}$, PVG/N$_2$C$_{0.5}$, and PVG/N$_2$C$_1$ were calculated to be 5.8 ± 0.14, 6.4 ± 0.62, 5.4 ± 0.22, 4.1 ± 0.26, and 2.2 ± 0.18 µm (Figure 1h), respectively.

2.2. Viscoelasticity, 3D Printing, and Mechanical Properties

Viscoelasticity is a crucial characteristic of hydrogel inks, particularly in 3D printing and bioprinting applications.[34] To evaluate the viscoelastic nature of the fabricated PVG/NC, we conducted the rheological examinations using a rotational rheometer with a 25 mm parallel plate at ambient conditions. Owing to the temperature-responsive gelation property of gelatin, we kept the PVG and its nanocomposite hydrogels at 4 °C for 30 min.[32,35] The hydrogels were tested under varying frequencies (0.1–100 Rad s^{-1}) to understand their self-healing and viscoelastic properties. Interestingly, all the hydrogels displayed a stable increase in storage modulus (G') with a decreasing loss modulus (G'') within a frequency range of 0.1–100 Rad s^{-1} (Figure S3a,b, Supporting Information), indicating the viscoelastic nature. As the CNC content increased in the PVG/CNT matrix, a gradual increase in storage modulus was observed. This is due to the rigid bonding between PVA/gelatin and interaction with CNT/CNCs, resulting in a highly viscoelastic hydrogel.[36] The G' value of the PVG, PVG/N$_2$C$_0$, PVG/N$_2$C$_{0.25}$, PVG/N$_2$C$_{0.5}$, and PVG/N$_2$C$_1$ hydrogel inks at high frequency (100 Rad s^{-1}) range was calculated to be 21 293, 25 580, 32 184, 34 638, and 36 448 Pa, respectively. Moreover, all the hydrogels exhibited a characteristic frequency-dependent change in viscosity (η^*) with an initial increase in viscosity (= elastic-like nature) at a low-frequency region (0.1 Rad s^{-1}), while a low viscosity (= viscous-like nature) in the high-frequency region (100 Rad s^{-1}) (Figure S3c, Supporting Information), indicating the elastic to viscous transition. The calculated viscosities for PVG, PVG/N$_2$C$_0$, PVG/N$_2$C$_{0.25}$, PVG/N$_2$C$_{0.5}$, and PVG/N$_2$C$_1$ hydrogel inks at 100 Rad/s were 213.04, 257.38, 323.94, 347.8, and 366.44 Pa.s. These results indicate that the PVG/NC hydrogel inks are highly viscoelastic, and the incorporation of borax/CNC/CNT enhanced the overall physical and chemical interaction of the resulting semi-inner penetrating polymer network (semi-IPN) hydrogels.[37]

To examine the shear-thinning behavior of the PVG/NC hydrogels, we next investigated the flow curve (viscosity vs shear rate), and the result is shown in **Figure 2a**. As expected, all the hydrogels displayed excellent shear-thinning properties within a shear range of 0.1–100 s^{-1}, meaning that the PVG/NC hydrogels have shear-induced deformation/reformation properties, ideal for 3D printing. The viscosities of the PVG, PVG/N$_2$C$_0$, PVG/N$_2$C$_{0.25}$, PVG/N$_2$C$_{0.5}$, and PVG/N$_2$C$_1$ hydrogel inks at low shear range (0.1 s^{-1}) were 4184.05, 7893.65, 11 312.42, 6879.81, and 5898.67 Pa.s, while at high shear range (100 s^{-1}) it was calculated to be 79.89, 95.84, 112.21, 53.27, and 59.71 Pa.s, respectively. We printed a 20 × 20 × 3 mm^3 square structure using PVG/N2C1 hydrogel ink to demonstrate the printing ability. Notably, the PVG/N$_2$C$_1$ ink displayed stable filament formation during printing, and the final printed structure is shown in Figure 2b. Based on this observation, we next aimed to investigate the high-resolution 3D printing ability of the PVG/N$_2$C$_1$ hydrogel ink using various geometric shapes, for example, hollow squares, hollow triangles, spiral patterns, and squares with wavy infill. As shown in Figure 2c and Movie S1 (Supporting Information), the hydrogel ink can accurately print geometric models. The printed hydrogel was able to maintain its structure without collapsing as it was layered, and it smoothly extruded from the needle. This demonstrates that the hydrogel can be printed in

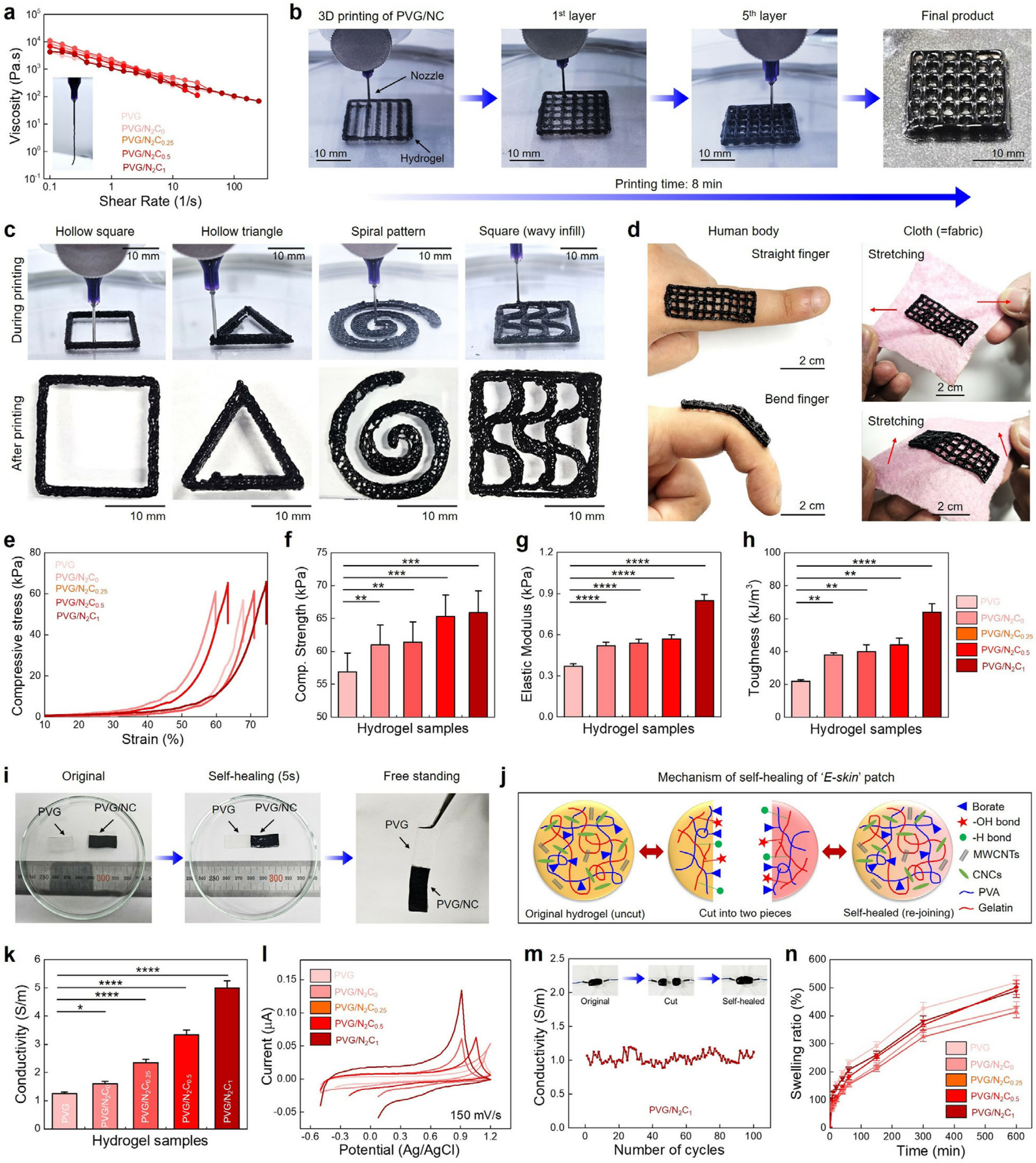

Figure 2. Physicochemical properties of the PVG/NC hydrogels. a) The shear-thinning behavior of the PVG and its nanocomposite hydrogels shows excellent viscoelasticity. b) Demonstration of 3D printing of PVG/N_2C_1 hydrogel ink using a direct ink writing (DIW) based 3D printer. scale bar: 10 mm. c) Printability test of the PVG/N_2C_1 using various geometries (hollow square, hollow triangle, spiral, and wavy pattern). scale bar: 10 mm. d) Digital photographs of the 3D printed PVG/NC "E-skin" patch attached to a human finger and fabric surface show good adhesion and stretchability. scale bar: 2 cm. e) Compressive stress-strain curve of the PVG and PVG/NC nanocomposite bulk hydrogel at room temperature. f–h) Calculation of compressive strength (kPa), elastic modulus (kPa), and toughness (kJ m^{-3}) of the hydrogels. i) Digital photographs of the self-healing test using PVG and PVG/N_2C_1 hydrogels. j) Schematic illustration of the self-healing mechanism of the PVG/NC hydrogel. k) Conductivity test of the bulk hydrogel samples showing an enhancement in electrical conductivity upon adding CNTs and CNCs. l) Cyclic voltammetry analysis of the PVG and PVG/NC hydrogels at a scan rate of 150 mV s^{-1} showing the oxidation-reduction potential. m) Cyclic stability of conductivity of the PVG/N_2C_1 hydrogels. n) Swelling properties of the fabricated hydrogel scaffolds at ambient temperature. Data reported as mean ± s.d. of triplicated ($n = 3$) experiments, statistical significance considered at $^{*}p < 0.05$, $^{***}p < 0.001$, and $^{****}p < 0.0001$ (One-way ANOVA test with Tukey's HSD *post-hoc* test).

appropriate sizes and shapes. This was due to the temperature-responsive property of gelatin and its ability to form sufficient hydrogen bonds with PVA and/or CNT/CNC. Moreover, we tested a big rectangular model (40 × 15 × 5 mm^3) to print and demonstrate the printability. As expected, the steady-state ink flow resulted in a good quality printing structure (Figure 2d), which was found adhesive, easily moldable, and stretchable when placed onto a human finger or cotton cloth (= fabric) surface, demonstrating its outstanding printability and durability.

To gain insight into the mechanical properties, we investigated the hydrogel's mechanical stability using a compressive test. Figure 2e illustrates the hydrogel's compressive strength as a strain function. With the addition of MWCNT, we observed an increase in compressive stress. Remarkably, the compressive strength gradually increased, and the peak height grew with higher CNC content (0 wt.% → 1 wt.%), indicating that MWCNT and/or CNC enhances the compressive strength of the hydrogel patches owing to the tough chemical bonding between PVA/gelatin with nanofillers.[38] Compared to the PVG, the compressive strength of PVG/N_2C_1 (strength: ≈65.89 ± 3.2 kPa) was significantly ($^{***}p < 0.001$) enhanced with an elastic modulus of ≈0.85 ± 0.05 kPa ($^{****}p < 0.0001$) and toughness of ≈64 ± 5.1 kJ m^{-3} ($^{****}p < 0.0001$), respectively (Figure 2f–h). Taken together, our results demonstrated that PVG/NC hydrogels are highly viscoelastic and printable and MWCNT/CNC significantly improved the mechanical strength, which would benefit skin adhesion and other downstream applications.

2.3. Self-Healing, Stretchability, and Conductivity of PVG/NC "E-Skin"

When borax is added as a crosslinker in the PVA matrix, it introduces a dynamic borate bond, leading to slime-like motion behavior with self-healing properties. The self-healing process occurs rapidly after the hydrogel is cut, taking less than 5 sec, as shown in Figure 2i, and chemically re-bonds strongly. The reattached hydrogel can stretch over 200 mm without breaking at the previously cut area (Figure S4, Supporting Information). In contrast, other parts of the hydrogel break under further stretching, indicating a rapid and robust self-healing ability. The mechanism behind the self-healing property is illustrated in Figure 2j. Nonetheless, the bulk PVG/N_2C_1 hydrogel patch exhibited exceptionally high stretchability in tensile mode, reaching 36 times its original shape (Figure S5, Supporting Information), further highlighting its superior stretchability.

Conductive hydrogels exhibiting elastic and self-healing properties hold significant potential for various applications in sensing, particularly for detecting motion and strain sensing.[1] In this regard, conductive nanofillers, such as MWCNT, play a crucial role in enhancing the electrical conductivity of biopolymer hydrogels, as they maintain an uninterrupted electron flow through filler-to-polymer-to-filler during strain sensing.[39] Moreover, CNCs with nanoscale dimensions and a high surface area-to-volume ratio act like electric dipoles, transmitting electrical signals between particles and sustaining an electroactivity state.[40] To evaluate the conductive properties of the fabricated PVG/NC "E-skin" patches, we performed the conductivity test using a digital multimeter, and the result is shown in Figure 2k. As expected, with the addition of MWCNT and CNC, the hydrogel electrical conductivity was increased synergistically as we move from PVG (≈1.25 ± 0.05 S m^{-1}) to PVG/N_2C_1 (≈5 ± 0.25 S m^{-1}) hydrogel. We further performed cyclic voltammetry (CV) measurements to find out the origin of the hydrogel's conductivity. Figure 2l illustrates the I–V curve of the developed nanocomposite hydrogels at a scan rate of 150 mV s^{-1}. The CV results for each sample in varying scan rates (25, 50, 100, and 150 mV s^{-1}) are also shown in Figure S6a–e (Supporting Information). These results highlight the changes in electrochemical properties with varying MWCNT and/or CNC content. The higher anodic current (I_{pa}) indicates a higher oxidation-reduction reaction through the hydrogel surface, indicating more excellent electrical conductivity. As CNC content increases, electrical conductivity improves, and the peaks of the PVG/N_2C_1 hydrogel showed a higher I_{pa} value (0.45 µA) than the PVG hydrogel (0.042 µA).

Among the various composites, the PVG/N_2C_1 hydrogel displayed good cyclic conductivity even after 100 cycles of breaking and re-joining the polymer chain (Figure 2m), further demonstrating the conductive property. This was also reflected in the self-healing and resistance change experiment. The resistance measurement of the self-healed hydrogel was conducted using uniform stretching. Digital photographs of the experiential process are shown in Figure S7a,b (Supporting Information). The hydrogel was stretched while measuring its resistance after cutting and re-joining the PVG and PVG/N_2C_1. The resistance increased from 4.51 to 11.39 kΩ as the hydrogel was stretched for 10 s, indicating that the molecular distance increases under strain, which reduces the distance between MWCNT and CNCs inside the PVG chains, leading to a reduction in electrical conductivity. The conductivity of hydrogels also depends on the wettability (= water holding capacity) of the hydrogels. All the hydrogels displayed desirable swelling under ambient conditions (Figure 2n), probably due to continuous electron flow during the oxidation-reduction reaction. This was also reflected in their long-term stability and conductivity. As shown in Figure S8a (Supporting Information), the PVG/NC hydrogels showed a more controlled degradation than PVG, with a slightly slow degradation of PVG/N_2C_1 after 7 d of incubation in 1 × PBS. The slow degradation rate of the PVG/NC hydrogels was due to the reduction of the hydrogel's porosity with increasing CNC content, suggesting the tougher polymeric structure formation and subsequent stability. Moreover, a conductivity test using PVG/N_2C_1 also suggested no change in conductivity. It illuminated an light emitting diode (LED) light properly even after keeping it for 7 d at ambient conditions (Figure S8b, Supporting Information), indicating its superior durability and conductivity, which would benefit long-term sensing applications.

2.4. Adhesive Test and Shape-Adaptability Property of PVG/NC "E-Skin"

One of the key features of hydrogel "E-skin" is its capacity to adhere to the skin and generate electrical signals for sensing devices.[41] Excellent adhesion ensures the versatility of hydrogel tape and improves sensing accuracy.[42] **Figure 3a** shows that PVG/N_2C_1 adheres well to glass, steel, plastic, wood, copper, paper, cotton, gloves, and skin. This demonstrates that it enables

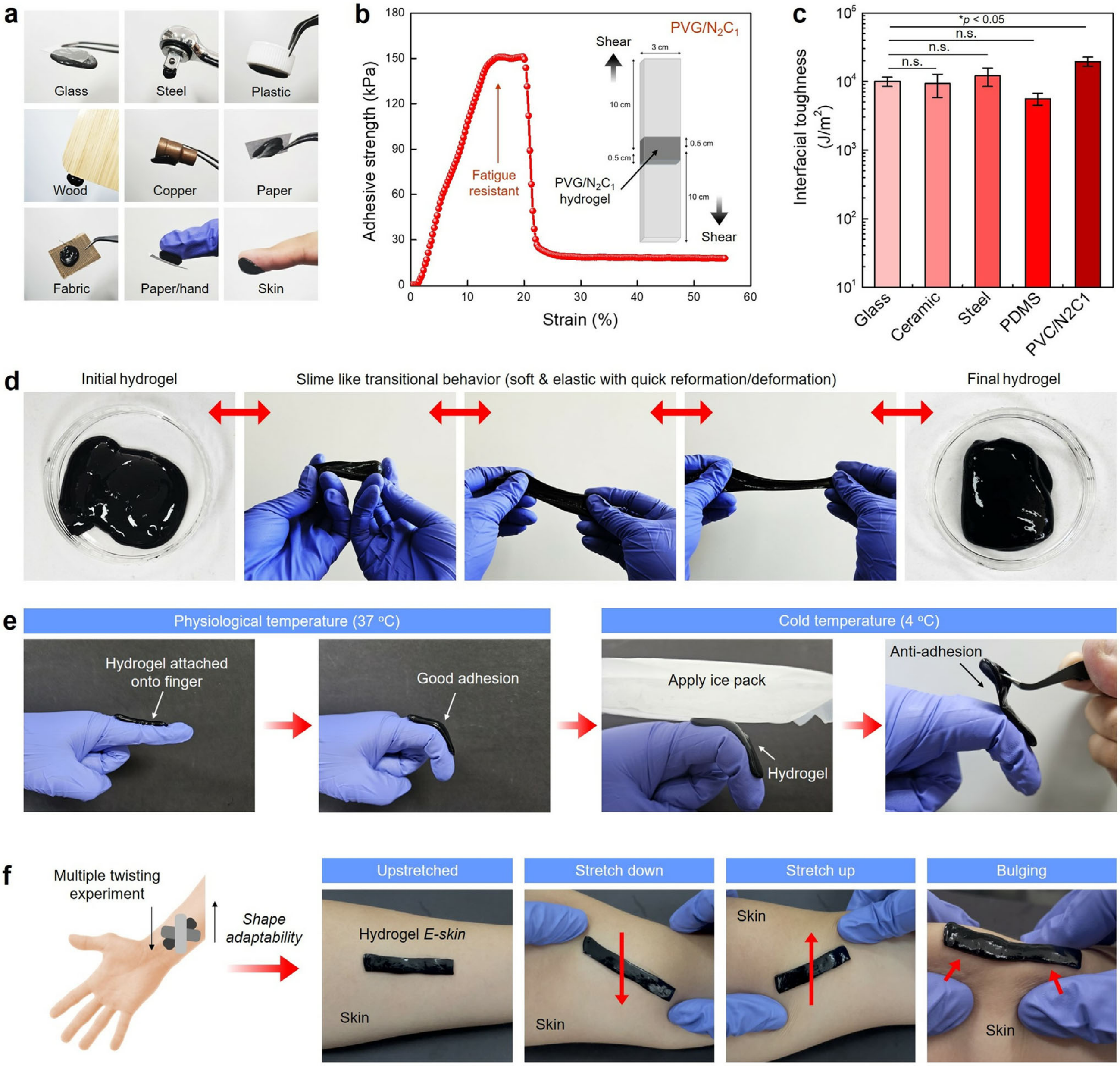

Figure 3. The adhesive property of the PVG/N_2C_1 slime "E-skin." a) Digital photographs showing the adhesion performance of PVG/N2C1 hydrogel on various surfaces (e.g., glass, steel, plastic, wood, copper, paper, fabric, and skin). b) The lap-shear adhesive strength of the PVG/N_2C_1 hydrogel. c) Comparison of interfacial toughness (J m^{-2}) of various materials vs PVG/N_2C_1 hydrogel. d) Digital photographs of the PVG/NC hydrogel showing the slime-like behavior during the reformation/deformation test. PVG/N_2C_1 can return to its original state even after being stretched and handled like a slime. e) Photographs showing the potential of PVG/N_2C_1 with adjustable adhesion based on temperature. f) PVG/NC remains firmly attached despite various movements, demonstrating excellent shape adaptability. Data reported as mean ± s.d. of triplicated ($n = 3$) experiments, statistical significance considered at $^{*}p < 0.05$ (One-way ANOVA test Tukey's HSD *post-hoc* test) while not significant data represented as *n.s.*

sensing on various surfaces, not just human skin. We selected only PVG/N_2C_1 hydrogel for adhesive and sensing experiments owing to its higher electrical conductivity among all composites. The lap-shear adhesion test was conducted to demonstrate the adhesive performance, and the experimental setup is shown in Figure S9 (Supporting Information). Notably, the PVG/N_2C_1 patch experiment showed that it could withstand forces up to 150 kPa before the adhesion failed (Figure 3b). The hydrogel can easily be adhered between the porcine skins, indicating its good adhesive behavior (Figure S10a,b, Supporting Information). Next, we performed an interfacial adhesion test, essential for any hydrogel's ultimate adhesion property. A pictorial demonstration and the interfacial adhesive force vs displacement curve are shown in Figure S10c (Supporting Information), deciphering the attachment of hydrogel to porcine skin and measuring the force required to detach it by pulling vertically. Thanks to its

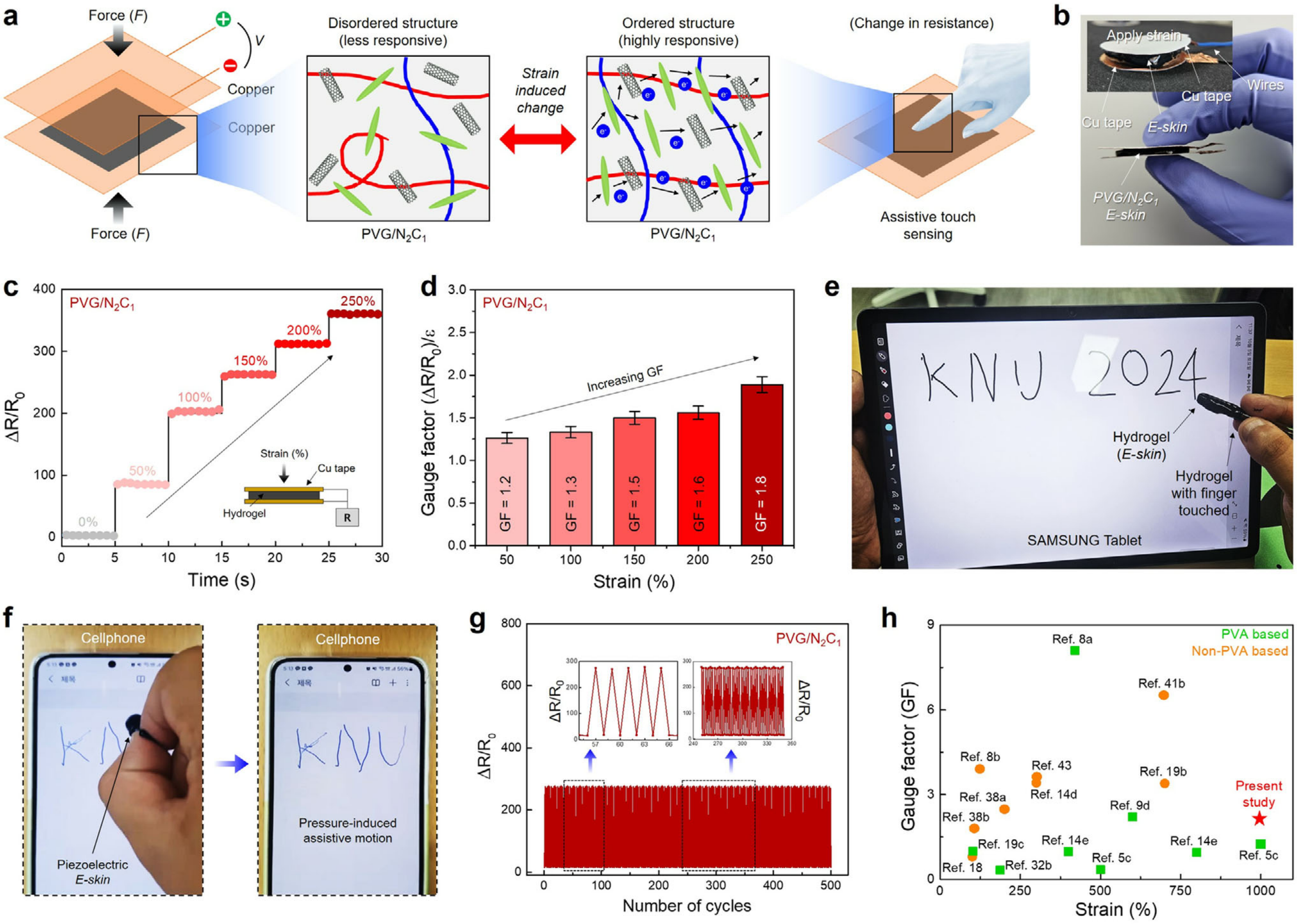

Figure 4. Pressure-responsive behavior of the PVG/NC slime-like "E-skin." a) Schematic illustration of the strain sensing experiment. PVG/N_2C_1 placed between thin copper tapes and the principle of its piezoelectric functionality. b) A photo of the setup used in the experiment, with wires connected to the copper tape for strain sensing. c) Change in resistance values with varying strain (0–250%) as a function of time. d) Calculation of gauge factor (GF) corresponding to the pressure changes. e) A tablet pen was created by attaching PVG/N_2C_1 to a glass rod, showing the pressure-responsive behavior. The hydrogel can be used as an "E-pen" for writing. f) Smartphone touch functionality test using PVG/N_2C_1. g) Cyclic resistance change stability after applying strain shows excellent strain–sensing properties. h) A comparative study on gauge factor vs strain of various PVA and non-PVA based hydrogels reported in the literature. Data reported as mean ± s.d. of triplicated ($n = 3$) experiments, statistical significance considered at $^*p < 0.05$ (One-way ANOVA test Tukey's HSD *post-hoc* test).

exceptional self-healing and excellent adhesiveness, PVG/NC hydrogel does not break even when subjected to impact or stretching. This allows it to adhere well to other hydrogel surfaces while remaining soft and elastic with an interfacial tensile strength of ≈120 ± 5.9 kPa, respectively. Our results showed that the interfacial toughness of the PVG/N_2C_1 "E-skin" patch (19 600 J m^{-2}) was significantly ($^*p < 0.05$) higher than glass, ceramic material, steel, and PDMS substrates,[43] demonstrating the outstanding adhesion ability (Figure 3c). Even after being handled and stretched, the hydrogel can quickly return to its original shape, as shown in Figure 3d indicating its slime-like motion behavior. Additionally, the adhesion strength of the hydrogel can be adjusted by temperature. When the hydrogel is attached to a finger, it remains securely in place even when it bends and flexes due to the body temperature (≈35 ± 2 °C). However, placing ice on the hydrogel lowers its temperature (≈10 ± 2 °C), causing it to harden and lose adhesion, making it easier to remove. This process is depicted in Figure 3e. To test the shape-adaptable feature and strain-induced anti-adhesion, we then test the adhesion ability of PVG/N2C1 the "E-skin" using human skin (= wrist). Figure 3f shows that the hydrogel remains firmly in place, even when the wrist is twisted or moved. This demonstrates that hydrogel can be attached to various body parts and stays secure even during vigorous movements.

2.5. Application of PVG/NC "E-Skin" in Human Body Sensing

Based on its excellent electrical conductivity, hydrogel demonstrates potential as a pressure (= strain) sensing platform. Applying pressure to the PVG/NC hydrogel generates resistance, enabling the detection of the magnitude and location of the applied pressure. The experimental setup and principle are shown in **Figure 4a**. We placed the PVG/N_2C_1 "E-skin" between thin copper tapes, with wires connected to each tape for easy measurement. A digital photograph of the experimental process is shown in

Figure 4b. Our results demonstrate that as the strain increased from 0 to 250%, a gradual increase in relative resistance was improved. It shows that resistance increases proportionally as pressure is applied, indicating a consistent rise (Figure 4c). The applied pressure enhanced the polymer chain mobility, allowing the rearrangement of the MWCNT and/or CNC particles inside the PVG matrix.[44] This was also reflected in the gauge factor (GF), a sensitivity indicator for measuring deformation in sensors like hydrogels. GF is calculated by dividing the change in resistance ($\Delta R/R_0$) by the strain. The results demonstrate that GF increases with applied pressure (Figure 4d). Due to its capability to measure microcurrent, the hydrogel can even operate a smartphone, which requires detecting subtle electrical currents from the hand. To validate this, a practical demonstration of the strain-induced current generation process is presented using a SAMSUNG tablet. As shown in Figure 4e and Movie S2 (Supporting Information), a glass rod was attached to the hydrogel to make it convenient to use as a tablet pen. The hydrogel's performance was also validated by using PVG/NC to write "KNU," representing Kangwon National University (Figure 4f; Movie S3, Supporting Information), "screen pattern unlocking," and "dial-up" on a smartphone screen, as shown in Movies S4,S5 (Supporting Information). To evaluate the durability of PVG/NC's strain-responsive functionality, pressure was applied 500 times. The results, illustrated in Figure 4g, indicate that the performance remains stable throughout repeated pressure applications, indicating the pressure-based sensitivity of the fabricated PVG/N_2C_1 "E-skin." A comparative study of strain-induced change in GF in various PVA based hydrogels reported in the literature is shown in Figure 4h.

The superior elasticity, self-healing, electroactive (electrochemical and strain sensing), and adhesive properties of the PVG/NC hydrogel "E-skin" could be an ideal platform for human motion sensing applications. Herein, we tested the feasibility of PVG/N_2C_1 "E-skin" on multiple human motion sensing. We tested the wrist, finger (straight and angular) bending, forehead, elbow movement, and voice control movement studies. Furthermore, the hand gesture sensing ability was also tested to check its feasibility for wearable sensing. We used the PVG/N_2C_1 gel owing to its superior adhesive and bioelectric properties. As depicted in **Figure 5**a,b, with prompt wrist and finger bending, a rapid change in relative resistance ($\Delta R/R_0$) was noticed up to five cycles. When the finger was straight, a stable resistance was recorded. As soon as the finger joint is moved vertically (up to 90°), a sharp increase in resistance was noted within a time frame of 0–35 s due to the separation and stretching of the polymer chain. This causes the MWCNT/CNC particles to move away in the polymer matrix, resulting in decreased current flow and increased resistance.

To verify this finding, we then tested the angular bending test of the finger starting from 0 to 90° bending point (Figure 5c). Interestingly, as the index finger was slowly moved downwards from 0–90° bending angles, a gradual increase in $\Delta R/R_0$ was observed in a time frame of 0–60 s with 5 times of cyclic stability, indicating the fast sensing ability of the PVG/N_2C_1 "E-skin." Similarly, we also found an increase in $\Delta R/R_0$ values when the forehead (3 cycles) and elbow (3 cycles) movement experiment was conducted (Figure 5d,f). Interestingly, the change in voice pattern can also be detected using our PVG/N_2C_1 hydrogel. As shown in Figure 5e, the PVG/N_2C_1 "E-skin" can quickly differentiate the voice pattern, e.g., "OK" and "BYE," when adhered to the throat, which can be detected by observing the change in $\Delta R/R_0$. These results demonstrate the outstanding sensing ability of the fabricated "E-skin" patch.

In addition, we also tested the hand gesture sensing ability up to 3 cycles with various gestures. For example, we selected the "HELLO 2024" gesture using various hand symbols and tried to sense them by observing the resistance change. The "H," "E," "L," "L," and "O" were defined by index-little fingers, index-middle-ring fingers, index-thumb fingers, and by closing the index-thumb fingers, respectively. Similarly, the "2024" gesture was created by gathering index-, middle-ring, small, thumb fingers. As shown in Figure 5g, the letter and number gestured can be detected very quickly by monitoring the change in resistance. Our results anticipate that electroactive PVG/NC hydrogel "E-skin" had better human body motion sensing ability under ambient conditions.

2.6. Humidity and Temperature Sensing

Owing to the presence of conductive nanofillers (MWCNTs and CNCs) and hydrated ion networks in PVG,[45] it can adsorb and release moisture in varying environmental conditions. For example, the winter, summer, and monsoon humidity and temperature varied differentially. Thus, the PVG/NC ionic "E-skin" with superior sensing ability would benefit environmental monitoring when adhered to the skin surface. **Figure 6**a schematically shows the varying humidity and temperature in all weather conditions. To test the feasibility of the hydrogel as a temperature sensor, we created various ionic solutions with varying (10, 30, 50, 70, and 80%) relative humidity (R.H.). Notably, the PVG/N_2C_1 "E-skin" smartly changes the resistance in contact to the increasing R.H. We observed that 80% R.H. has a more significant change in resistance compared to the 10% R.H. (Figure 6b). In addition, the resistance change was linearly correlated with the increasing R.H. with an R^2 value of 0.97, indicating suitable humidity sensing (Figure 6c). To verify this finding, we next inserted the PVG/N_2C_1 "E-skin" inside a commercial 3M face mark and evaluated the human breathing pattern. Briefly, the hydrogel tape was adhered inside the face mask using copper tape with two wires, ensuring strong support (Figure 6d). As the face mask with hydrogel patch was put on, the PVG/N_2C_1 "E-skin" quickly detected the breathing pattern by identifying the moisture obtained inside. We observed a relative resistance change when humans start slow and fast breathing during inhalation and exhalation (Figure 6e). The change in resistance of the implanted PVG/N_2C_1 patch can be explained by the change in temperature (~1.7 °C) during inhalation and exhalation of air during fast breathing. **Figure S11** shows that exhaled airflow (≈36.8 °C) was slightly higher than the inhaled air (≈35.1 °C), causing moisture loss and creating a force towards the hydrogel patch, thus increasing resistance value. The real-time temperature sensing ability of the PVG/N_2C_1 "E-skin" was studied by adhering the hydrogel tape onto the glass beaker filled with water and a digitally controlled heating system. It was worth noticing that the hydrogel's resistance increased significantly as the water beaker warmed to

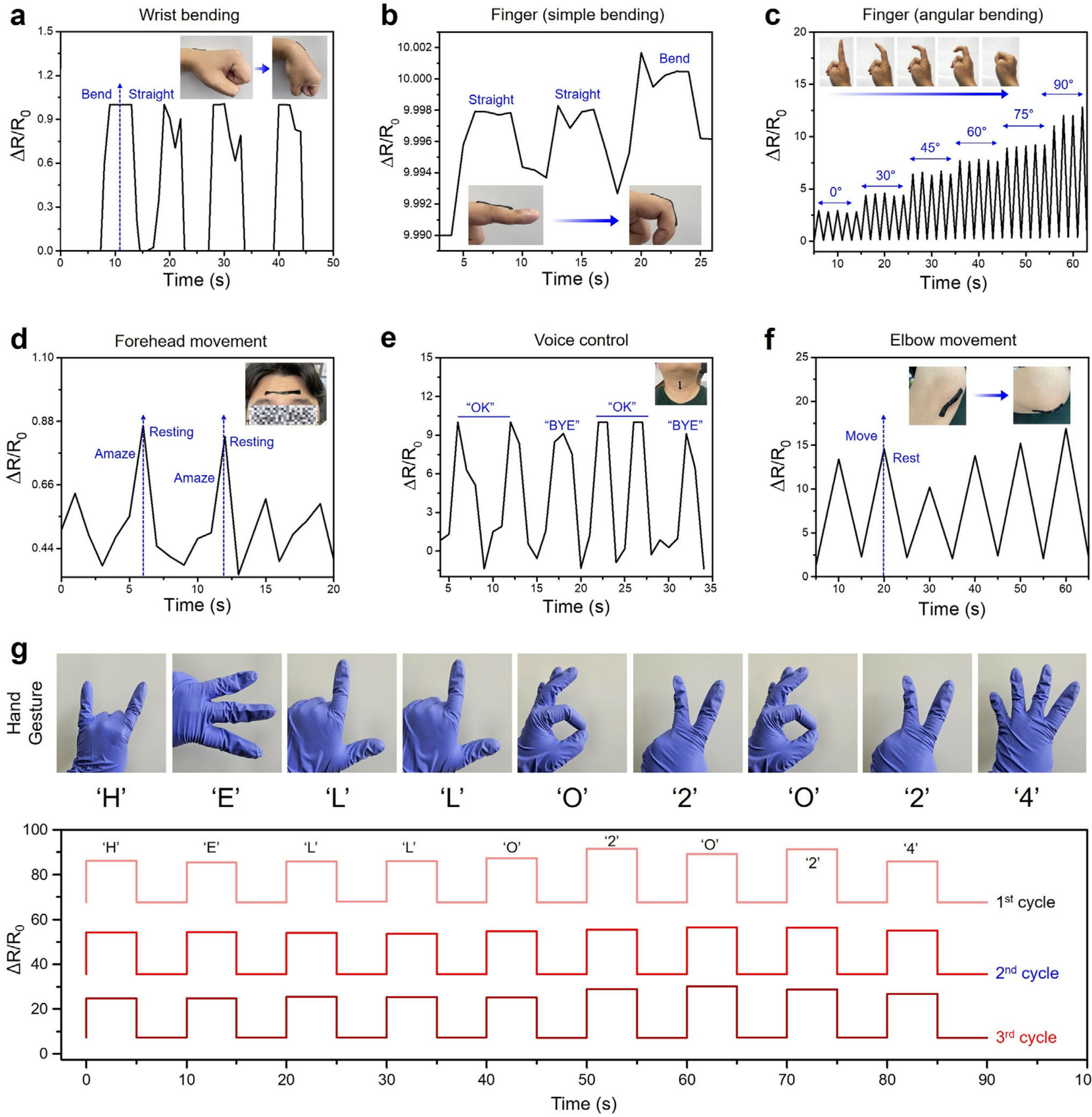

Figure 5. Application of PVG/N_2C_1 "E-skin" on human body motion and strain sensing applications. a–c) The real-time detection of wrist and finger bending by examining the change in resistance. d–f) The real-time forehead, elbow, and voice control sensing ability of the "E-skin" patch. g) Demonstration of real-time hand gesture sensing ability of the PVG/N_2C_1 hydrogel patch by using a letter (HELLO) and number (2024) sensing.

60 ± 2 from 10°. The change in relative resistance with corresponding thermal images is shown in Figure 6f. The experimental photograph is shown in Figure 6g. With the increasing temperature, the hydrogel tape loses the moisture content, making it less electroactive and increasing the $\Delta R/R_0$ value. A schematic illustration of the mechanism of temperature and humidity-induced hydrogel sensing is shown in Figure 6h.

2.7. In Vitro Photothermal, Antibacterial, and Biocompatibility Evaluation

The in vitro antibacterial and biocompatibility tests were conducted to evaluate the biosafety of the hydrogel "E-skin" patch. Owing to the near-infrared (NIR)-responsive property of MWCNT,[46] the antibacterial test was performed w/ or w/o NIR irradiation. To test the NIR-responsive properties of the

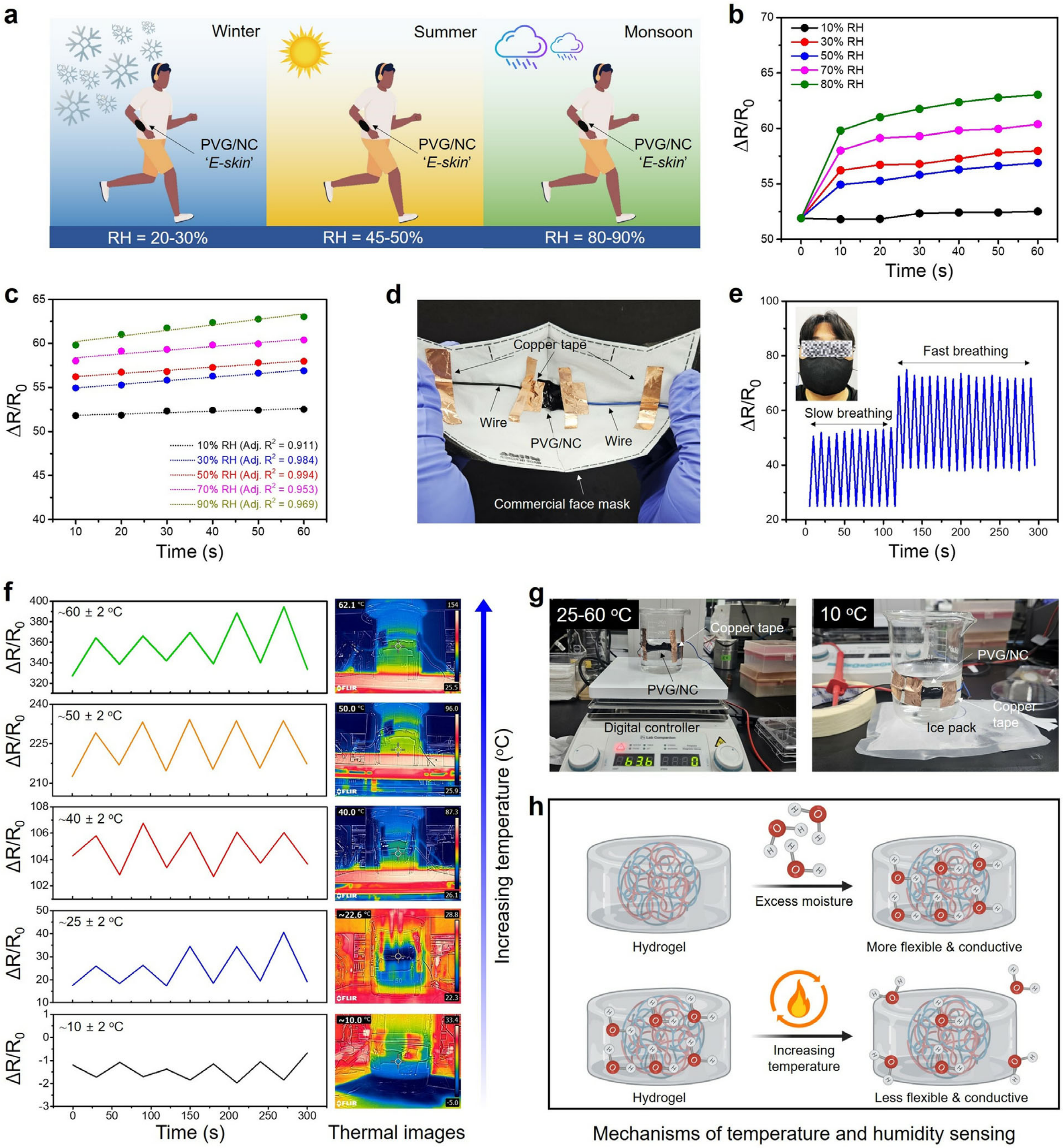

Figure 6. Application of PVG/N_2C_1 "E-skin" on real-time humidity and temperature sensing. a) Schematic diagram for the change of relative humidity (R.H.) in winter, summer, and monsoon. b) The change in relative resistance in 10–80% R.H. within a time frame of 0–60 s. c) Linearity curve for the humidity sensing for PVG/N_2C_1 "E-skin." d,e) Real-time human breath pattern monitoring using PVG/N_2C_1 "E-skin" patch. f,g) Real-time temperature sensing ability of the PVG/N_2C_1 "E-skin" patch. h) Schematic illustration showing the mechanism of temperature and humidity sensing.

hydrogels, we examine the time-dependent temperature rise profiles. We used 808 nm NIR at 0.5 W cm^{-2} density. As expected, the PVG/N_2C_0 and PVG/N_2C_1 hydrogels displayed a time-dependent temperature rise to 80 °C (**Figure 7a**), comparable with previous literature.[47] In contrast, the pure PVG and D.W. showed no visible increase in temperature within a time frame of 0 to 5 min. The NIR thermal images of the hydrogels are shown in Figure 7b. The PVG/N_2C_1 hydrogel displayed good photothermal stability after three NIR on-off cycles, indicating its photothermal stability (Figure 7c).

Inspired by the outstanding NIR-responsive properties, we performed the antibacterial test using the fabricated hydrogels. The antibacterial performance was monitored by dilution plate culture assay and anti-biofilm assay. We used E. coli and MRSA

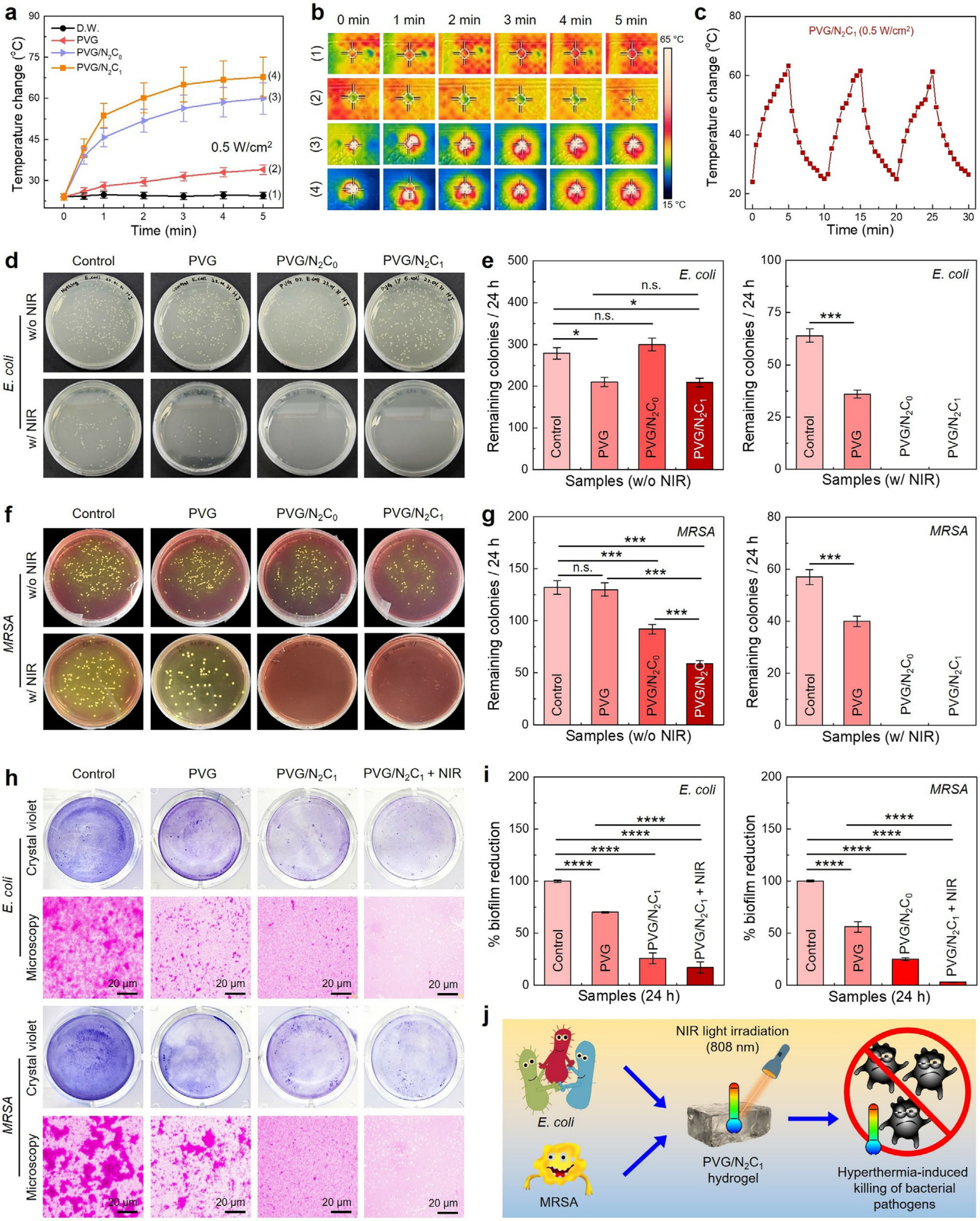

Figure 7. In vitro NIR-responsive antibacterial performance of the PVG/NC "E-skin" patch. a) Representative near-infrared (NIR) light-responsive properties of the PVG/NC hydrogels. The graph shows the NIR light irradiation dose-dependent temperature rise profile for PVG, PVG/N$_2$C$_0$, and PVG/N$_2$C$_1$

as a model gram-negative and positive bacterium that causes skin infections. As shown in Figure 7d,f, both the E. coli and MRSA showed a high growth w/o NIR in PVG hydrogel and a little in PVG/NC hydrogel. Interestingly, w/ NIR, both the E. coli and MRSA showed a dramatic decrease in colony formation after 24 h, indicating the efficient killing under the influence of NIR light. The outstanding antibacterial performance was due to the NIR-triggered hyperthermia and reactive oxygen species (ROS) generation,[48] which successfully inhibited the bacteria growth. The statistical data of the colony formation is shown in Figure 7e, g. As illustrated, the NIR-irradiated PVG/N_2C_1 group exhibited a significantly ($^{***}p < 0.001$) reduced number of colony formation after 24 h for both E. coli and MRSA. We also performed the biofilm formation assay to verify these findings using the crystal violet staining method. As depicted in Figure 7h, both E. coli and MRSA biofilm formation efficiency was significantly reduced after NIR treatment with PVG/N_2C_0 and PVG/N_2C_1, with a high reduction in crystal violet stain in the PVG/N_2C_1 group. The quantification results of the biofilm formation assay also reflected a similar pattern. The percentage of biofilm reduction (Figure 7i) for E. coli and MRSA was found to be significantly ($^{****}p < 0.0001$) higher for PVG/N_2C_1 + NIR group, suggesting their antibacterial potential. A schematic illustration of the mechanism of the antibacterial effect is shown in Figure 7j. Skin bioelectronics must have desirable biocompatibility to commercialize the product.[49] To verify that the skin cells are biocompatible with the fabricated "E-skin," we tested the cytotoxicity of HaCaT cells using water-soluble tetrazolium-8 (WST-8) and live/dead assay. As shown in Figure S12 (Supporting Information), the HaCaT cells were highly biocompatible with all the fabricated hydrogels after 24 h of in vitro culture. In particular, the viability percentage in HaCaT cells was significantly ($^{**}p < 0.01$) higher in PVG/NC groups than in control, suggesting that all the formulations were highly cytocompatible. The live/dead staining assay also supported this, and the result is shown in **Figure 8**. Notably, all the hydrogels were found biocompatible with the HaCaT cell culture for 24 h, and the PVG/NC patches showed higher cell growth, suggesting their exceptional biocompatibility. Taken together, our results demonstrate that PVG/NC slime-like "E-skin" is moldable, printable, and highly biocompatible with outstanding antibacterial properties, which could help develop clinical-grade wound healing patches for multiplex biosensing and tissue regeneration.

3. Conclusion

In summary, we developed a bioinspired hydrogel-based "E-skin" patch with printable and highly conductive properties. We incorporated gelatin and PVA as flexible and adhesive polymer matrix and CNC/CNT as conductive nanofiller and mechanical reinforcement. The as-fabricated "E-skin" patch exhibited high stretchability (≈1000%), stretching ≈36 times the original length, superior electrical conductivity (≈5 ± 0.25 S/m), and self-healing properties, ideal for soft bioelectronics development. Additionally, using a novel method of freeze-thawing and dynamic crosslinking (physical and chemical) followed by 3D printing enabled good printability and biocompatibility. The fabricated "E-skin" patch demonstrated exceptional sensitivity towards human body motion, temperature, and humidity sensing. Due to its self-healing effect, the patch can be reused multiple times, maintaining stable sensing performance even after more than 100 cycles of cutting and reattachment. Moreover, owing to the NIR-responsive properties, the PVG/NC hydrogel "E-skin" prevented pathogenic bacterial growth on the hydrogel with repeated use, suggesting its multifunctional abilities. Furthermore, the hydrogels were found to be highly biocompatible with HaCaT cells. Thus, our developed PVG/NC "E-skin" patch shows excellent potential in healthcare monitoring and could be used as an ideal wound healing patch in clinical settings.

4. Experimental Section

Materials: Polyvinyl alcohol (PVA, 1500 MW, > 99%, Daejung, Republic of Korea), gelatin Type-A form porcine skin (purity: ≥ 98%; gel strength ≈300 g bloom, Sigma-Aldrich, USA), and multi-walled carbon nanotubes (MWCNTs, Applied Carbon Nano, Republic of Korea) were obtained from commercial vendors. Cellulose nanocrystals (CNCs) were synthesized from filter paper using acid hydrolysis, as reported in our previous literature. Sodium tetraborate anhydrous (Borax, 99.5%) was obtained from Alfa Aesar, Massachusetts, USA. The chemicals were used as received without any further purification unless stated elsewhere. Deionized water (D.I., 18.2 Mohm.cm, Millipore) was used for all the experiments.

Fabrication of Multifunctional Hydrogel Patch: For hydrogel fabrication, the first 1 g (10 w/v %) of PVA was dissolved in 10 mL of D.I. water at 90 °C under constant stirring (300 rpm) for 4 h. After complete dissolution, 0.5 g (5 w/v %) of gelatin was added, and the solution was stirred overnight at 45–50 °C. The next day, 0.03 g of MWCNTs (2 wt.%) was added to the resulting mixture. 2 wt.% MWCNTs were chosen for all the hydrogels owing to their superior biocompatibility (≈76.31% viability of skin cells) as investigated by the WST-8 assay. Consequently, CNCs at varying concentrations (0%, 0.25%, 0.5%, 1% wt.%) were added to the PVA/gelatin/MWCNT mixture. Afterward, the nanocomposite pre-hydrogel solution was stirred overnight and crosslinked using sodium tetraborate ($Na_2B_4O_7$) solution. The borax solution was prepared at a concentration of 0.04 M L^{-1},[31] and 2 per 10 mL of hydrogel solution was added for crosslinking. After adding the borax solution, the mixture was quickly stirred with a glass rod to ensure thorough blending. The resulting hydrogel was either cut into sizes suitable for each experiment or molded into specific shapes using molds. For 3D printing, the hydrogel solution was loaded into a printing cartridge without borax crosslinking and was subjected to a freeze-thawing technique to achieve physically crosslinked printable inks.

hydrogels (808 nm, 0.5 W cm^{-2}, 5 min). b) NIR thermal images of the hydrogels up to 5 min at 0.5 W cm^{-2}. c) Temperature stability of the PVG/N2C1 hydrogel after three successive NIR on/off cycles. d,f) Digital photographs of the plate dilution test assay showing the antibacterial efficiency of the fabricated hydrogel patches against E. coli (gram-negative) and MRSA (gram-positive) w/ or w/o NIR light treatment. e,g) Statistical analysis of the colony formation test. h) Anti-biofilm formation assay of E. coli and MRSA after 24 h in the presence of fabricated PVG/N_2C_1 hydrogel w/ or w/o NIR. Digital photographs of the crystal violet stained plates with corresponding optical microscopy images showing the presence of biofilm. scale bar: 20 µm. i) Statistical analysis of the anti-biofilm test. j) Schematic illustration of the NIR-triggered and hyperthermia-induced antibacterial properties of the PVG/NC hydrogel. Data reported as mean ± s.d. of triplicated ($n = 3$) experiments, statistical significance considered at $^{*}p < 0.05$, $^{***}p < 0.001$, and $^{****}p < 0.0001$ (One-way ANOVA test with Tukey's HSD *post-hoc* test).

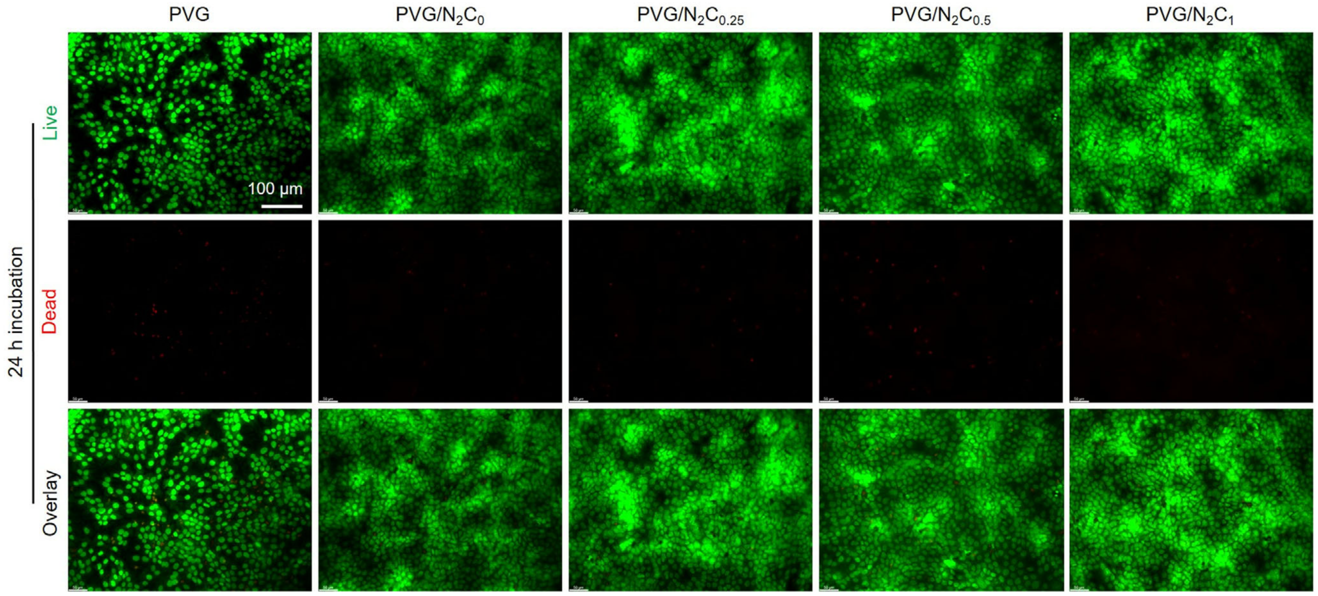

Figure 8. In vitro biocompatibility of the fabricated slime-like hydrogels. Representative fluorescence microscopy images of the HaCaT cells show the live (green) and dead (red) cells after 24 h incubation with various hydrogels. scale bar: 100 µm.

3D Printing: The 3D printing was carried out using the CELLINK Bio X (Cellink, Gothenburg, Sweden). The 3D model was designed using AutoCAD software (Autodesk, Mill Valley, United States) and exported as a Stereolithography (STL) file. For 3D printing, various CAD models, such as square ($20 \times 20 \times 5$ mm^3, with varying infill and pattern), hollow triangle and rectangle (20×5 mm^2), and spiral (20×5 mm^2) were used. After 3D printing, the hydrogels were kept at 4 °C until further use. Printing was performed at room temperature using a single-nozzle (21 G, 0.51 mm) hydrogel cartridge (3 mL, pneumatic) at a speed of 2 mm s^{-1} under an extrusion pressure of 80 ± 5 kPa.

Characterizations—General Characterization: The morphology of the CNCs and CNTs was investigated using a transmission electron microscope (TEM; JEM-2100F, Jeol, Japan), and the particle size distribution was measured using ImageJ (v1.8.0, NIH, Bethesda, USA) software. FT–IR spectroscopy (Frontier, Perkin Elmer, UK) was employed to evaluate the chemical interactions within the hydrogel across a wavelength range of 4000–500 cm^{-1}, with a resolution of 4 cm^{-1}. A total of 32 measurements were conducted. Structural modifications in the hydrogels were observed using X-ray diffraction (XRD; X'Pert PRO MPD, Philips, Eindhoven, Netherlands) with Cu Kα radiation (λ = 1.5414 Å), operating at 40 kV and 40 mA. The surface morphology of the 3D printed samples was analyzed using a scanning electron microscope (SEM) (Hitachi-S4800, Tokyo, Japan) with an acceleration voltage of 5.0 kV. Before the SEM analysis, the printed samples were freeze-dried for two days using a freeze dryer (EYELA Freeze Drying Unit 2200, Tokyo, Japan) and coated with platinum. The equipment employed in this experiment was a universal testing machine (UTM; MCT-1150, A&D, Co. Japan), and it was operated using the associated software, MSAT-Lite. The compression was carried out at a speed of 10 mm min^{-1}.

Characterizations—Evaluation of Mechanical Properties: Mechanical strength tests were conducted using a tensile compression tester (MCT-1150, Shimadzu, Kyoto, Japan). This equipment measured the compressive strength of five hydrogels with varying CNC and/or CNT ratios. All hydrogels were molded into spherical shapes (1.5×1 cm^2) with a consistent weight of 3 g before being compressed. The elastic modulus was calculated by dividing the compressive strength by the strain.

Characterizations—Adhesive Test: The adhesive properties of the PVG/N$_2$C$_1$ were assessed using lap-shear and interfacial adhesive tests under ambient conditions according to the guidelines of the American Society for Testing and Materials (ASTM)–F2458–05 and ASTM–F2258, respectively. For the lap-shear adhesive test, PVG/N$_2$C$_1$ hydrogel (≈100 mg) was placed inside two overlapped rectangular cardboards (10×3 cm^2 each), and the adhesive strength was measured in tensile mode. For the interfacial adhesive test, one acrylic plate was covered with pig (= porcine) skin while another was coated with the PVG/N$_2$C$_1$ hydrogel ($2 \times 2 \times 0.5$ cm^3, ≈500 mg). These two plates were then pulled in the vertical direction using a tensile tester. The tensile strength for interfacial adhesive test was calculated using the following Equation (1):

$$\text{Tensile strength}\ \left(TS_{\text{interfacial}}\right) = \frac{F_{max}}{W\ \times L}) \tag{1}$$

F$_{max}$, W, and L indicated the sample's maximum force at shear, width, and length. Additionally, the PVG/N$_2$C$_1$ hydrogel was attached to various materials, including glass, steel, plastic, wood, copper, paper, cotton, gloves, and human skin, to evaluate its macroscopic adhesion performance across different surfaces and photographed. The multiple adhesive and twisting experiments were conducted using PVG/N$_2$C$_1$ hydrogel ($2 \times 0.5 \times 0.1$ cm^3) attached to the human hand and subsequently photographed.

Characterizations—Self-Healing and Stretchability Tests: A self-healing test was conducted using easily distinguishable hydrogels, one containing 2 wt.% MWCNT + 1 wt.% CNC (PVG/N$_2$C$_1$) in black color and the other without CNT/CNC in transparent form (pure PVG). Two hydrogel pieces, each cut into rectangles of ≈20 mm, were placed together. After waiting for 10 s, the self-healing and stretchability were assessed by pulling from both sides. Moreover, we also tested the stretchability of the PVG/NC hydrogel ($57 \times 19 \times 0.7$ cm^3) in tensile mode using ASTM-D638-14 standards. The self-healed hydrogel was stretched over 20 cm to verify strong adhesion, and the hydrogel's electrical conductivity was assessed by measuring resistance changes after repeatedly cutting and self-healing up to 100 times.

Characterizations—Swelling and Degradation Study: The swelling and degradation tests were conducted using freeze-dried hydrogel scaffolds. For the swelling test, the fabricated hydrogel scaffolds ($5 \times 5 \times 1$ cm^3) were immersed in 1× PBS (5 mL) at 37 °C for various time points, and the dry weight (W$_d$) of each scaffold was recorded. The scaffold samples were removed from PBS at the desired time interval, and the excess water was carefully blotted. Then, the swollen weight (Ws) was recorded. The percentage of swelling was calculated using the following Equation (2):

$$\%\ \text{swelling} = \frac{W_s - W_d}{W_d} \times 100\% \tag{2}$$

For the degradation test, the hydrogels were placed in 1 × PBS for 7 d at 37 °C, and their weight was measured daily at a set time after removing excess moisture and complete drying.

Electrochemical and Sensing Analysis: A multimeter and a source meter were used for the conductivity tests. The conductive properties of the hydrogels were measured from the slope of the current-voltage (IV) curves using a Source meter (Keithley 2400, Keithley Instruments, Ohio, USA) at ambient temperature. Conductivity was determined using the following Equation (3):

$$L = \frac{1}{\rho} = \frac{1}{RS} \tag{3}$$

where L, ρ, R, and S indicated the hydrogel sample's conductivity, resistivity, resistance, and cross-sectional area.

A digital multimeter (Fluke 17B+, Fluke Corporation, Washington, USA) was used by taking a rectangular hydrogel ($2 \times 1 \times 0.5$ cm^3) for simple resistance measurements. Electrical conductivity for each CNC ratio was determined by measuring cyclic voltammetry using a source meter, and based on these results, the hydrogel with the highest conductivity (= PVG/N_2C_1) was selected for sensing tests.

Electrochemical and Sensing Analysis—Real-Time Human Body Motion Sensing: The hydrogel "E-skin" ($2 \times 0.5 \times 0.1$ cm^3) was attached to the wrist, fingers, forehead, neck, and elbows for body motion sensing. Subsequently, electrical stimulation was applied with a current of 0.5 mA and a voltage of 15 mV by connecting wires for a 1 min test duration. The joints were flexed and extended during the experiment, while the hydrogel attached to the eyebrows was tested through facial grimaces. Additionally, to achieve more detailed sensing, resistance changes were measured according to the degree of finger bending and the different shapes of the fingers. The relative change in resistance ($\Delta R/R_0$) was evaluated by using the following Equation (4):

$$\left(\Delta \frac{R}{R_0}\right) = \frac{R_s - R_0}{R_0} \times 100\% \tag{4}$$

R_0 and R_s were the PVG/N_2C_1 hydrogel resistance before and after strain measurement. The strain sensing performance of the PVG/N_2C_1 hydrogel was measured using gauge factor (GF) under varying strain (50–250%). The GF was calculated according to the following Equation (5):

$$\text{Gauge factor (GF)} = \frac{\text{Change in resistance}}{\varepsilon} \tag{5}$$

where ϵ was the applied strain on the hydrogel. For body motion sensing experiments, the Dean of the Department of Biosystems Engineering at Kangwon National University took and approved the written consent of human volunteers.

Electrochemical and Sensing Analysis—Real-Time Humidity Sensing: For humidity sensing, the hydrogel "E-skin" ($2 \times 0.5 \times 0.1$ cm^3) was kept in a chamber with varying humidity (e.g., 10, 30, 50, 70, and 80%), and the relative change in resistance ($\Delta R/R_0$) was recorded. For practical demonstration, the PVG/N_2C_1 hydrogel "E-skin" ($2 \times 2 \times 0.1$ cm^3) was wired with copper tape and then attached to a commercial facemask (3M) to evaluate changes in resistance ($\Delta R/R_0$) due to humidity from exhalation.

Electrochemical and Sensing Analysis—Real-Time Temperature Monitoring: For temperature sensing, the hydrogel "E-skin" ($2 \times 0.5 \times 0.1$ cm^3) was attached to a beaker filled with water ranging from 10 to 60 °C, and the change in resistance was measured according to temperature. The strain-responsive nature of the PVG/N_2C_1 was tested by placing the hydrogel (2×0.5 cm^2) between thin copper tapes and applying pressure by hand.

Measurement of Photothermal Properties: The photothermal properties of the PVG, PVG/N_2C_0, and PVG/N_2C_1 hydrogels were measured in ambient conditions. For this, hydrogel samples (≈50 mg) were taken in 96-well plates and irradiated with an 808 NIR light source (MDL-H-808-5 W, Changhun New Industries Optoelectronics Tech. Co., China) with a power density of 0.5 W cm^{-2} up to 5 min. The temperature change was recorded using a NIR thermal camera. The temperature stability of the PVG/N_2C_1 hydrogel was also monitored at 0.5 W cm^{-2} power density after three heating–cooling cycles.

Antibacterial Studies: The antibacterial test of the fabricated hydrogel samples was assessed using a dilution plate and biofilm formation assays. Escherichia coli (E. coli, gram-negative) and methicillin-resistant Staphylococcus aureus (MRSA, gram-positive) were used and obtained from the American Type Culture Collection (ATCC, USA). The antibacterial experiment was conducted by irradiating the bacteria samples (E. coli and MRSA) with an 808 nm NIR light source at 0.5 W cm^{-2} for 5 min.

Antibacterial Studies—Dilution Plate Assay: For this, E. coli and MRSA were incubated in nutrient agar (Sigma-Aldrich, USA) and tryptic soy broth (Sigma-Aldrich, USA) for 24 h at 37 °C with constant stirring. The viability of $OD_{600} = 0.1$–0.3 for each bacteria was subsequently used for antibacterial assays. For dilution plate assay, the bacteria solution (1×10^6 CFU mL^{-1}, 100 µL for 5 mL of total volume) was mixed with the hydrogel samples and incubated at 37 °C for 24 h. Next, the PVG/N_2C_0 and PVG/N_2C_1 samples were irradiated with 808 nm NIR light (0.5 W cm^{-2}) for 5 min under sterile conditions. After that, serial dilution was performed, and 50 µL of bacteria (both E. coli and MRSA) was plated using nutrient agar (E. coli) and tryptic soy agar (MRSA) and additionally cultured for 24 h. After 24 h, the reduction in bacterial colony was photographed, and the remaining colonies were counted using ImageJ software (v1.8.0, NIH, Bethesda, USA). Plates without hydrogel were considered a negative control, while PVG-treated samples were a positive control. The data was represented as mean ± s.d. of triplicated ($n = 3$) experiments.

Antibacterial Studies—Biofilm Formation Assay: For this, per-diluted (1×10^6 CFU mL^{-1}) bacterial solution (both E. coli and MRSA) was incubated in a 24-well (1 mL well^{-1}) plate for 2 d in static condition at 37 °C to generate visible biofilms. After that, the hydrogel samples were then taken into each well and cultured for 6 h. After the desired culture, the hydrogels were irradiated with 808 nm NIR light (0.5 W cm^{-2}) for 5 min under sterile conditions. Subsequently, after NIR treatment, the hydrogel samples were removed, and the remaining biofilms were washed carefully with PBS and stained with 0.5% crystal violet (Sigma-Aldrich, USA) for 10 min. After desirable staining, the plates were washed with PBS, and the biofilm formation was photographed. To quantify the biofilm formation, 95% ethanol was added to each well, and the residual stain was collected, followed by recording the absorbance value at 590 nm using a spectrophotometer. Plates without hydrogel were considered a negative control, while PVG-treated samples were a positive control. The data was represented as mean ± s.d. of triplicated ($n = 3$) experiments.

In Vitro Biocompatibility Study: The human keratinocyte cells (HaCaT) were obtained from the Korean Cell Line Bank (KCLB), Seoul National University, Republic of Korea. The HaCaT cell was cultured in DMEM (Welgene, Republic of Korea) media, supplemented with 10% fetal bovine serum (FBS, Sigma-Aldrich, USA) and 1% Antibiotic–Antimycotic (Thermo Scientific, USA). A culture medium containing ≈100 mg of hydrogel was added to the plate along with the cells (≈1.5×10^4/100 µL/96-well plate), and the cells were incubated for 24 h. After incubation, 10 µL of WST-8 reagent (Cellrix, MediFab, Republic of Korea) was added, and the samples were incubated for 2 h. After 2 h, the cells' optical density (O.D.) was measured spectrometrically. For live/dead assay, the HaCaT cells were incubated with hydrogels in 24-well plates (≈4×10^4/1 mL well^{-1}) for 24 h, followed by incubation of live/dead assay dye (Thermo Fischer Scientific, USA). After the desired staining, the cell images were captured using an inverted fluorescence microscope (DMi8 Series, Leica, Germany) with a 20 × objective lens and applying proper filter channels. The data was represented as mean ± s.d. of triplicated ($n = 3$) experiments.

Statistical Analysis: The statistical analysis used Origin Pro v9.1 (Origin Labs, USA). The statistical significance between the control and experimental groups was analyzed using the One-way Analysis of Variance (ANOVA) with Tukey's HSD *post-hoc* test. Data reported as mean ± s.d. of triplicated ($n = 3$) experiments, and statistical significance was considered at $^{*}p < 0.05$, $^{***}p < 0.001$, and $^{****}p < 0.0001$. LAS-X (v1.4.7, Leica, Germany) and ImageJ (v1.8.0, NIH, USA, https://imagej.net/ij/) were used to quantify FE–SEM and fluorescence images. At least three (n = 3) independent images from each group were assessed for quantification analysis.

Supporting Information

Supporting Information is available from the Wiley Online Library or from the author.

Acknowledgements

The Basic Science Research Program supported this work through the National Research Foundation of Korea (Grant Nos. RS-2018-NR031068 and RS-2022-NR075661), Republic of Korea. Additionally, this work received support from the Innovative Human Resource Development for Local Intellectualization program through the Institute of Information & Communications Technology Planning & Evaluation (IITP) grant, which is funded by the Korean government (MSIT) (IITP-2025-RS-2023-00260267).

Conflict of Interest

The authors declare no conflict of interest

Author Contributions

H.K. and S.D.D. contributed equally to this work. H.K. contributed to conceptualization, methodology, formal analysis, writing the original draft, reviewing and editing, and software. S.D.D. contributed to conceptualization, methodology, formal analysis, writing the original draft, reviewing and editing, project administration, and supervision. M.J.J. contributed to methodology, formal analysis, visualization, and validation. J.L. and H.P. contributed to writing, reviewing and editing, as well as software. Y.S. contributed to methodology and formal analysis. K.-T. L. contributed to writing, review and editing, supervision, project administration, and funding acquisition.

Data Availability Statement

The data that support the findings of this study are available from the corresponding author upon reasonable request.

Keywords

3D printing and healthcare monitoring, antibacterial, bioadhesives, bioelectronics, flexible E-skin

Received: February 14, 2025
Revised: March 23, 2025
Published online:

---

[1] a) H. Li, J. Cao, R. Wan, V. R. Feig, C. M. Tringides, J. Xu, H. Yuk, B. Lu, *Adv. Mater.* **2024**, 2415151; b) W. Li, J. Liu, J. Wei, Z. Yang, C. Ren, B. Li, *Adv. Funct. Mater.* **2023**, *33*, 2213485; c) W. Cui, Y. Zheng, R. Zhu, Q. Mu, X. Wang, Z. Wang, S. Liu, M. Li, R. Ran, *Adv. Funct. Mater.* **2022**, *32*, 2204823; d) Y. Feng, H. Liu, W. Zhu, L. Guan, X. Yang, A. V. Zvyagin, Y. Zhao, C. Shen, B. Yang, Q. Lin, *Adv. Funct. Mater.* **2021**, *31*, 2105264; e) G. Li, C. Li, G. Li, D. Yu, Z. Song, H. Wang, X. Liu, H. Liu, W. Liu, *Small* **2022**, *18*, 2101518.

[2] a) J. Wang, Y. Qi, Y. Gui, C. Wang, Y. Wu, J. Yao, J. Wang, *Small* **2024**, *20*, 2305951; b) Z. Wang, N. Li, X. Yang, Z. Zhang, H. Zhang, X. Cui, *Microsyst. Nanoeng.* **2024**, *10*, 55; c) S. Zhuo, A. Tessier, M. Arefi, A. Zhang, C. Williams, S. K. Ameri, *npj Flexible Electron.* **2024**, *8*, 49; d) L. Zhang, S. Xing, H. Yin, H. Weisbecker, H. T. Tran, Z. Guo, T. Han, Y. Wang, Y. Liu, Y. Wu, *Nat. Commun.* **2024**, *15*, 4777; e) F. Ershad, S. Patel, C. Yu, *npj Flexible Electron.* **2023**, *7*, 32; f) Y. Guo, Y. Wang, Q. Tong, B. Shan, L. He, Y. Zhang, D. Wang, *npj Flexible Electron.* **2024**, *8*, 25; g) E. Bihar, E. J. Strand, C. A. Crichton, M. N. Renny, I. Bonter, T. Tran, M. Atreya, A. Gestos, J. Haseloff, R. R. McLeod, *npj Flexible Electron.* **2023**, *7*, 48; h) Z. Pang, Y. Zhao, N. Luo, D. Chen, M. Chen, *Nanomaterials* **2022**, *12*, 2522.

[3] a) Y. Shin, H. S. Lee, J.-U. Kim, Y.-H. An, Y.-S. Kim, N. S. Hwang, D.-H. Kim, *Biomaterials* **2025**, *314*, 122802; b) S. H. D. Wong, G. R. Deen, J. S. Bates, C. Maiti, C. Y. K. Lam, A. Pachauri, R. AlAnsari, P. Bělský, J. Yoon, J. M. Dodda, *Adv. Funct. Mater.* **2023**, *33*, 2213560; c) W. Liu, R. Xie, J. Zhu, J. Wu, J. Hui, X. Zheng, F. Huo, D. Fan, *npj Flexible Electron.* **2022**, *6*, 68; d) J. Wen, J. Tang, H. Ning, N. Hu, Y. Zhu, Y. Gong, C. Xu, Q. Zhao, X. Jiang, X. Hu, *Adv. Funct. Mater.* **2021**, *31*, 2011176.

[4] a) W. Shi, H. Li, C. Xu, G. Wu, J. Chen, J. Zhang, L. Liang, Q. Wu, Y. Liang, G. Li, *npj Flexible Electron.* **2024**, *8*, 82; b) M. Kim, M. Cho, C. Chung, K.-U. Kyung, *npj Flexible Electron.* **2024**, *8*, 59; c) J. Song, Y. Zhang, S. Y. Chan, Z. Du, Y. Yan, T. Wang, P. Li, W. Huang, *npj Flexible Electron.* **2021**, *5*, 26.

[5] a) S. Liu, Y. Wu, L. Jiang, W. Xie, B. Davis, M. Wang, L. Zhang, Y. Liu, S. Xing, M. D. Dickey, *ACS Appl. Mater. Interfaces* **2024**, *16*, 46538; b) P. Wang, G. Li, J. Liu, Z. Hou, C. Meng, S. Guo, C. Liu, S. Fan, *Adv. Mater. Interfaces* **2021**, *8*, 2100998; c) S. Azadi, S. Peng, S. A. Moshizi, M. Asadnia, J. Xu, I. Park, C. H. Wang, S. Wu, *Adv. Mater. Technol.* **2020**, *5*, 2000426.

[6] S. Zheng, L. Ruan, F. Meng, Z. Wu, Y. Qi, Y. Gao, W. Yuan, *Small* **2024**, 2408745.

[7] a) Y. Guo, X. Wei, S. Gao, W. Yue, Y. Li, G. Shen, *Adv. Funct. Mater.* **2021**, *31*, 2104288; b) G. B. Pradhan, S. Jeong, S. Sharma, S. Lim, K. Shrestha, Y. Lee, J. Y. Park, *Adv. Funct. Mater.* **2024**, *34*, 2407978.

[8] a) W. Dai, J. Wang, K. Xiang, W. Hu, J. Sun, H. Zhang, L. Wang, *ACS Appl. Mater. Interfaces* **2023**, *15*, 29499; b) Z. Wang, H. Zhou, W. Chen, Q. Li, B. Yan, X. Jin, A. Ma, H. Liu, W. Zhao, *ACS Appl. Mater. Interfaces* **2018**, *10*, 14045.

[9] a) P. GhavamiNejad, A. GhavamiNejad, H. Zheng, K. Dhingra, M. Samarikhalaj, M. Poudineh, *Adv. Healthcare Mater.* **2023**, *12*, 2202362; b) Z. Shen, Z. Zhang, N. Zhang, J. Li, P. Zhou, F. Hu, Y. Rong, B. Lu, G. Gu, *Adv. Mater.* **2022**, *34*, 2203650; c) J.-Y. Gong, F.-C. Sun, Y.-C. Pan, A.-M. Fei, S.-F. Leicheng, F.-P. Du, Y.-F. Zhang, *Mater. Today Commun.* **2022**, *33*, 104324; d) X. Peng, W. Wang, W. Yang, J. Chen, Q. Peng, T. Wang, D. Yang, J. Wang, H. Zhang, H. Zeng, *J. Colloid Interface Sci.* **2022**, *618*, 111.

[10] a) X. Ju, J. Kong, G. Qi, S. Hou, X. Diao, S. Dong, Y. Jin, *Nat. Commun.* **2024**, *15*, 762; b) M. A. Zahed, M. Sharifuzzaman, H. Yoon, M. Asaduzzaman, D. K. Kim, S. Jeong, G. B. Pradhan, Y. D. Shin, S. H. Yoon, S. Sharma, *Adv. Funct. Mater.* **2022**, *32*, 2208344; c) W. Wang, H. Zhou, Z. Xu, Z. Li, L. Zhang, P. Wan, *Adv. Mater.* **2024**, 2401035; d) Q. T. Lai, X. H. Zhao, Q. J. Sun, Z. Tang, X. G. Tang, V. A. Roy, *Small* **2023**, *19*, 2300283; e) Y. Hu, F. Wang, H. Ye, J. Jiang, S. Li, B. Dai, J. Li, J. Yang, X. Song, J. Zhang, *npj Flexible Electron.* **2024**, *8*, 30.

[11] a) Y. Wang, P. Zhu, M. Tan, M. Niu, S. Liang, Y. Mao, *Adv. Intell. Syst.* **2023**, *5*, 2300162; b) X. Liu, H. Li, M. Tao, Y. Yu, Z. Zhu, D. Wu, X. Hu, Y. Chen, *Adv. Mater. Technol.* **2024**, 2400661; c) J. Du, G. Fu, X. Xu, A. M. Elshahawy, C. Guan, *Small* **2023**, *19*, 2207833.

[12] C. Wang, T. Yokota, T. Someya, *Chem. Rev.* **2021**, *121*, 2109.

[13] a) S. D. Dutta, D. K. Patel, K.-T. Lim, *J. Biol. Eng.* **2019**, *13*, 55; b) Z. Wang, M. Zhu, J. Li, C. Hu, J. Li, R. Xiong, C. Huang, *Nano Energy* **2024**, 109974.

[14] a) H. Kim, S. D. Dutta, A. Randhawa, T. V. Patil, K. Ganguly, R. Acharya, J. Lee, H. Park, K.-T. Lim, *Int. J. Biol. Macromol.* **2024**, 130732;

b) Y. Tong, C. Jiang, C. Ji, W. Liu, Y. Wang, *Small* **2025**, *21*, 2407956; c) M. J. Jeon, A. Randhawa, H. Kim, S. D. Dutta, K. Ganguly, T. V. Patil, J. Lee, R. Acharya, H. Park, Y. Seol, *Adv. Healthcare Mater.* **2025**, *14*, 2403983; d) X. Yao, S. Zhang, L. Qian, N. Wei, V. Nica, S. Coseri, F. Han, *Adv. Funct. Mater.* **2022**, *32*, 2204565; e) Y. Zhou, C. Wan, Y. Yang, H. Yang, S. Wang, Z. Dai, K. Ji, H. Jiang, X. Chen, Y. Long, *Adv. Funct. Mater.* **2019**, *29*, 1806220.

[15] Q. Li, C. He, C. Wang, Y. Huang, J. Yu, C. Wang, W. Li, X. Zhang, F. Zhang, G. Qing, *Small* **2023**, *19*, 2207932.

[16] F. Hao, X. Maimaitiyiming, S. Sun, *Macromol. Chem. Phys.* **2023**, *224*, 2200272.

[17] a) A. Khan, N. Nichakornpong, T. Wongsalam, P. Prathumrat, C. Likitaporn, P. Kasemsiri, M. Okhawilai, *Sci. Rep.* **2024**, *14*, 29715; b) L. He, D. Di, X. Chu, X. Liu, Z. Wang, J. Lu, S. Wang, Q. Zhao, *J. Controlled Release* **2023**, *363*, 180.

[18] F. Mo, Y. Huang, Q. Li, Z. Wang, R. Jiang, W. Gai, C. Zhi, *Adv. Funct. Mater.* **2021**, *31*, 2010830.

[19] a) Z. Deng, T. Hu, Q. Lei, J. He, P. X. Ma, B. Guo, *ACS Appl. Mater. Interfaces* **2019**, *11*, 6796; b) X. Sun, Z. Qin, L. Ye, H. Zhang, Q. Yu, X. Wu, J. Li, F. Yao, *Chem. Eng. J.* **2020**, *382*, 122832; c) L.-Y. Hsiao, L. Jing, K. Li, H. Yang, Y. Li, P.-Y. Chen, *Carbon* **2020**, *161*, 784; d) M. Liao, P. Wan, J. Wen, M. Gong, X. Wu, Y. Wang, R. Shi, L. Zhang, *Adv. Funct. Mater.* **2017**, *27*, 1703852.

[20] a) A. Dalla Colletta, M. Pelin, S. Sosa, L. Fusco, M. Prato, A. Tubaro, *Carbon* **2022**, *196*, 683; b) L. Ding, J. Stilwell, T. Zhang, O. Elboudwarej, H. Jiang, J. P. Selegue, P. A. Cooke, J. W. Gray, F. F. Chen, *Nano Lett.* **2005**, *5*, 2448.

[21] J. W. Kim, H. Park, G. Lee, Y. R. Jeong, S. Y. Hong, K. Keum, J. Yoon, M. S. Kim, J. S. Ha, *Adv. Funct. Mater.* **2019**, *29*, 1905968.

[22] Y. Hui, Y. Yao, Q. Qian, J. Luo, H. Chen, Z. Qiao, Y. Yu, L. Tao, N. Zhou, *Nat. Electron.* **2022**, *5*, 893.

[23] a) J. Li, J. Cao, R. Bian, R. Wan, X. Zhu, B. Lu, G. Gu, *Nat. Commun.* **2025**, *16*, 185; b) H. Liu, C. Du, L. Liao, H. Zhang, H. Zhou, W. Zhou, T. Ren, Z. Sun, Y. Lu, Z. Nie, *Nat. Commun.* **2022**, *13*, 3420.

[24] K. Wu, J. Li, Y. Li, H. Wang, Y. Zhang, B. Guo, J. Yu, Y. Wang, *Adv. Funct. Mater.* **2024**, 2404451.

[25] S. Roy, K. A. Deo, H. P. Lee, J. Soukar, M. Namkoong, L. Tian, A. Jaiswal, A. K. Gaharwar, *Adv. Funct. Mater.* **2024**, 2313575.

[26] a) A. Andreu, H. Lee, J. Kang, Y. J. Yoon, *Adv. Funct. Mater.* **2024**, 2315046; b) S. Zhou, Y. Zhao, Y. Xun, Z. Wei, Y. Yang, W. Yan, J. Ding, *Chem. Rev.* **2024**, *124*, 3608; c) D. Song, X. Chen, M. Wang, Z. Wu, X. Xiao, *Chem. Eng. J.* **2023**, 146011; d) R. Su, J. Chen, X. Zhang, W. Wang, Y. Li, R. He, D. Fang, *Small* **2023**, *19*, 2206391.

[27] a) J. Heikenfeld, A. Jajack, J. Rogers, P. Gutruf, L. Tian, T. Pan, R. Li, M. Khine, J. Kim, J. Wang, *Lab Chip* **2018**, *18*, 217; b) J. H. Lee, K. Cho, J. K. Kim, *Adv. Mater.* **2024**, *36*, 2310505; c) W. D. Li, K. Ke, J. Jia, J. H. Pu, X. Zhao, R. Y. Bao, Z. Y. Liu, L. Bai, K. Zhang, M. B. Yang, *Small* **2022**, *18*, 2103734; d) L. Xiang, X. Zeng, F. Xia, W. Jin, Y. Liu, Y. Hu, *ACS Nano* **2020**, *14*, 6449.

[28] a) S. D. Dutta, K. Ganguly, A. Randhawa, T. V. Patil, D. K. Patel, K.-T. Lim, *Biomaterials* **2023**, *294*, 121999; b) A. B. Bello, D. Kim, D. Kim, H. Park, S.-H. Lee, *Tissue Eng., Part B* **2020**, *26*, 164.

[29] K. Alim, N. Andrew, A. Pringle, *Curr. Biol.* **2013**, *23*, R1082.

[30] D. K. Patel, S. D. Dutta, J. Hexiu, K. Ganguly, K.-T. Lim, *Int. J. Biol. Macromol.* **2020**, *162*, 1429.

[31] H. Yu, L. Zhao, L. Wang, *J. Appl. Polym. Sci.* **2023**, *140*, 53852.

[32] a) S. D. Dutta, J. Hexiu, D. K. Patel, K. Ganguly, K.-T. Lim, *Int. J. Biol. Macromol.* **2021**, *167*, 644; b) S. A. Fraser, W. E. Van Zyl, *Macromol. Mater. Eng.* **2022**, *307*, 2100973.

[33] R. M. Abdelaziz, A. El-Maghraby, W. A.-A. Sadik, A.-G. M. El-Demerdash, E. A. Fadl, *Sci. Rep.* **2022**, *12*, 6424.

[34] S. D. Dutta, K. Ganguly, A. Randhawa, T. Patil, D. K. Patel, K.-T. Lim, *Biomaterials* **2023**, 121999.

[35] a) P. Singh, H. Baniasadi, S. Gupta, R. Ghosh, S. Shaikh, J. Seppälä, A. Kumar, *Int. J. Biol. Macromol.* **2024**, *278*, 134402; b) S. Asim, T. A. Tabish, U. Liaqat, I. T. Ozbolat, M. Rizwan, *Adv. Healthcare Mater.* **2023**, *12*, 2203148.

[36] I. C. Moraes, R. A. Carvalho, A. M. Q. Bittante, J. Solorza-Feria, P. J. Sobral, *J. Food Eng.* **2009**, *95*, 588.

[37] C. Shao, L. Meng, M. Wang, C. Cui, B. Wang, C.-R. Han, F. Xu, J. Yang, *ACS Appl. Mater. Interfaces* **2019**, *11*, 5885.

[38] a) M. Wu, X. Wang, Y. Xia, Y. Zhu, S. Zhu, C. Jia, W. Guo, Q. Li, Z. Yan, *Nano Energy* **2022**, *95*, 106967; b) D. Hardman, T. G. Thuruthel, F. Iida, *NPG Asia Mater.* **2022**, *14*, 11.

[39] X. Li, Y. Yang, B. Xie, M. Chu, H. Sun, S. Hao, Y. Chen, Y. Chen, *Adv. Mater. Technol.* **2019**, *4*, 1800476.

[40] a) S. D. Dutta, T. V. Patil, K. Ganguly, A. Randhawa, R. Acharya, M. Moniruzzaman, K.-T. Lim, *Carbohydr. Polym.* **2023**, *320*, 121232; b) D. K. Patel, K. Ganguly, S. D. Dutta, T. V. Patil, A. Randhawa, K.-T. Lim, *Int. J. Biol. Macromol.* **2023**, *229*, 105.

[41] a) H. Y. Yuen, H. P. Bei, X. Zhao, *Chem. Eng. J.* **2022**, *431*, 133372; b) X. Li, Z. Liu, Y. Liang, L.-M. Wang, Y. D. Liu, *J. Mater. Chem. B* **2022**, *10*, 3434.

[42] a) T. Nezakati, A. Seifalian, A. Tan, A. M. Seifalian, *Chem. Rev.* **2018**, *118*, 6766; b) B. Yin, M. Gosecka, M. Bodaghi, D. Crespy, G. Youssef, J. M. Dodda, S. H. D. Wong, A. B. Imran, M. Gosecki, A. Jobdeedamrong, *Chem. Eng. J.* **2024**, 150403; c) W. Zheng, W. Yang, W. Wei, Z. Liu, P. L. Tremblay, T. Zhang, *Adv. Healthcare Mater.* **2024**, *13*, 2303138; d) D. K. Patel, E. Jung, S. Priya, S.-Y. Won, S. S. Han, *Carbohydr. Polym.* **2024**, *323*, 121408.

[43] H. Yuk, C. E. Varela, C. S. Nabzdyk, X. Mao, R. F. Padera, E. T. Roche, X. Zhao, *Nature* **2019**, *575*, 169.

[44] H. Lin, W. Yuan, W. Zhang, R. Dai, T. Zhang, Y. Li, S. Ma, S. Song, *Carbohydr. Polym.* **2025**, *348*, 122781.

[45] X. Jing, H. Li, H.-Y. Mi, Y.-J. Liu, P.-Y. Feng, Y.-M. Tan, L.-S. Turng, *Sens. Actuators, B* **2019**, *295*, 159.

[46] B. Han, Y. L. Zhang, Q. D. Chen, H. B. Sun, *Adv. Funct. Mater.* **2018**, *28*, 1802235.

[47] Z. Sobhani, M. A. Behnam, F. Emami, A. Dehghanian, I. Jamhiri, *Int. J. Nanomed.* **2017**, 4509.

[48] Z. M. Markovic, L. M. Harhaji-Trajkovic, B. M. Todorovic-Markovic, D. P. Kepić, K. M. Arsikin, S. P. Jovanović, A. C. Pantovic, M. D. Dramićanin, V. S. Trajkovic, *Biomaterials* **2011**, *32*, 1121.

[49] J. Chen, F. Liu, T. Abdiryim, X. Liu, *Adv. Compos. Hybrid Mater.* **2024**, *7*, 35.